MusE gas flow and wind (MEGAFLOW) VIII: discovery of a MgII emission halo probed by a quasar sightline

Zabl, J.; Bouché, N.F.; Wisotzki, L.; Schaye, J.; Leclercq, F.; Garel, T.; ... ; Richard, J.

MNRAS 000, 1–22 (2020) Preprint 1 June 2021 Compiled using MNRAS LATEX style file v3.0

MusE GAs FLOw and Wind (MEGAFLOW) VIII. Discovery of a Mg II emission halo probed by a quasar sightline

Johannes Zabl,[1,2⋆] Nicolas F. Bouché,[1] Lutz Wisotzki,[3] Joop Schaye,[4] Floriane Leclercq,[5] Thibault Garel,[5,1] Martin Wendt,[6,3] Ilane Schroetter,[7] Sowgat Muzahid,[8,3] Sebastiano Cantalupo,[9] Thierry Contini,[10] Roland Bacon,[1] Jarle Brinchmann,[4,11] Johan Richard[1]

[1] Univ Lyon, Univ Lyon1, Ens de Lyon, CNRS, Centre de Recherche Astrophysique de Lyon UMR5574, F-69230 Saint-Genis-Laval, France
[2] Institute for Computational Astrophysics and Department of Astronomy & Physics, Saint Mary's University, 923 Robie Street, Halifax, Nova Scotia, B3H 3C3, Canada
[3] Leibniz-Institut für Astrophysik Potsdam (AIP), An der Sternwarte 16, 14482 Potsdam, Germany
[4] Leiden Observatory, Leiden University, PO Box 9513, NL-2300 RA Leiden, the Netherlands
[5] Observatoire de Genève, Université de Genève, 51 Ch. des Maillettes, 1290 Versoix, Switzerland
[6] Institut für Physik und Astronomie, Universität Potsdam, Karl-Liebknecht-Str. 24/25, 14476 Golm, Germany
[7] GEPI, Observatoire de Paris, CNRS-UMR8111, PSL Research University, Univ. Paris Diderot, 5 place Jules Janssen, 92195 Meudon, France
[8] IUCAA, Post Bag-04, Ganeshkhind, Pune, India - 411007
[9] Department of Physics, ETH Zürich,Wolfgang-Pauli-Strasse 27, 8093 Zürich, Switzerland
[10] Institut de Recherche en Astrophysique et Planétologie (IRAP), Université de Toulouse, CNRS, UPS, F-31400 Toulouse, France
[11] Instituto de Astrofísica e Ciências do Espaço, Universidade do Porto, CAUP, Rua das Estrelas, PT4150-762 Porto, Portugal

Accepted XXX. Received YYY; in original form ZZZ

ABSTRACT

Using deep (11.2 hr) VLT/MUSE data from the MEGAFLOW survey, we report the first detection of extended Mg II emission from a galaxy's halo that is probed by a quasar sightline. The Mg II $\lambda\lambda$ 2796, 2803 emission around the $z = 0.702$ galaxy ($\log(M_*/\mathrm{M}_\odot) = 10.05^{+0.15}_{-0.11}$) is detected out to ≈ 25 kpc from the central galaxy and covers 1.0×10^3 kpc^2 above a surface brightness of 14×10^{-19} erg s^{-1} cm^{-2} arcsec^{-2} ($2\,\sigma$; integrated over 1200 km s^{-1} = 19Å and averaged over 1.5 arcsec^2). The Mg II emission around this highly inclined galaxy ($i \simeq 75$deg) is strongest along the galaxy's projected minor axis, consistent with the Mg II gas having been ejected from the galaxy into a bi-conical structure. The quasar sightline, which is aligned with the galaxy's minor axis, shows strong Mg II absorption ($EW_0^{\lambda 2796} = 1.8$ Å) at an impact parameter of 39 kpc from the galaxy. Comparing the kinematics of both the emission and the absorption - probed with VLT/UVES -, to the expectation from a simple toy model of a bi-conical outflow, we find good consistency when assuming a relatively slow outflow ($v_{\mathrm{out}} = 130$ km s^{-1}). We investigate potential origins of the extended Mg II emission using simple toy models. With continuum scattering models we encounter serious difficulties in explaining the luminosity of the Mg II halo and in reconciling density estimates from emission and absorption. Instead, we find that shocks might be a more viable source to power the extended Mg II (and non-resonant [O II]) emission.

Key words: galaxies: evolution – galaxies: haloes – intergalactic medium – quasars: absorption lines – quasars: individual: SDSSJ0937+0656

1 INTRODUCTION

There is a substantial body of indirect observational evidence that galaxy evolution is controlled by the interplay between galaxies and their surrounding circum-galactic medium (CGM). Galaxies need to accrete gas - the fuel for star formation - from the circumgalactic medium, as the amount of gas inside a galaxy at a given time is not sufficient to explain the build up of their total stellar mass (e.g. Daddi et al. 2010; Tacconi et al. 2010, 2013; Freundlich et al.

⋆ E-mail: johanneszabl@gmail.com

2013; Saintonge et al. 2013). Once formed, massive stars will end up as supernovae and power large-scale outflows.

The low density CGM is traditionally studied through the absorption it imprints on background sources. The background sources can be either the associated galaxies themselves (down-the-barrel) or unassociated background sources (transverse sightlines). Through collecting large samples of sightlines, *statistical* insights into the distribution, physical state, and kinematics of the CGM gas can be gained. These samples have revealed a complex multi-phase CGM (see Tumlinson et al. 2017 for a recent review).

The resonant Mg II $\lambda\lambda$2796, 2803 doublet is an especially useful tracer of the cool (10^{4-5} K) and metal enriched CGM due to its strength and rest-wavelength, which allows to study it with ground-based optical spectroscopy for redshifts between $0.3 \lesssim z \lesssim 2.5$.

Studies with transverse quasar sightlines have revealed that Mg II is not isotropically distributed around galaxies, but is instead found preferentially along the galaxy minor or major axis (e.g. Bordoloi et al. 2011; Bouché et al. 2012; Kacprzak et al. 2012; Lan et al. 2014; Nielsen et al. 2015; Martin et al. 2019; Schroetter et al. 2019; Zabl et al. 2019). Down-the-barrel observations also support this conclusion (e.g. Bordoloi et al. 2014). This bi-modality is consistent with a simple picture where galaxies are surrounded by extended gas disks, from which they likely accrete gas, and supernova driven winds that are ejected into a bi-conical outflow launched perpendicular to the disk. The kinematics of both the presumed disk sightlines (Steidel et al. 2002; Chen et al. 2005; Kacprzak et al. 2010, 2011; Bouché et al. 2013, 2016; Ho et al. 2017; Ho & Martin 2020; Rahmani et al. 2018a; Zabl et al. 2019) and the presumed outflow sightlines (e.g. Bouché et al. 2012; Kacprzak et al. 2014; Muzahid et al. 2015; Schroetter et al. 2015, 2016, 2019; Rahmani et al. 2018b; Martin et al. 2019; Zabl et al. 2020) are in good agreement with this simple picture.

Compared to transverse sightlines, down-the-barrel observations have the advantage that the sign of the velocity is known, but they have the major disadvantage that the location of the Mg II absorbing gas is not directly constrained, and could thus be ISM (inter-stellar medium), CGM or even IGM (inter-galactic medium) gas. Blue-shifted Mg II absorption, which definitely represents outflows, is common in down-the-barrel observations and is strongest for galaxies that are observed face-on (e.g. Weiner et al. 2009; Rubin et al. 2010), but the observed absorption strength does not only depend on inclination, but also on other - non-geometric - properties such as stellar mass, star-formation density, and redshift (e.g. Martin et al. 2012; Rubin et al. 2014).

Another complication with down-the-barrel absorption studies is infilling by ISM Mg II *emission*. While more massive star-forming galaxies ($\log(M_*/\mathrm{M}_\odot) \gtrapprox 10.0$) appear to show mainly Mg II absorption with little or no emission, lower-mass galaxies ($\log(M_*/\mathrm{M}_\odot) \lessapprox 9.0$) appear to show only emission, with intermediate-mass galaxies between these masses showing P-Cygni profiles (e.g. Finley et al. 2017b; Feltre et al. 2018). These variations in Mg II are possibly a consequence of the complex radiative transfer that the resonant Mg II doublet experiences in the ISM gas (Prochaska et al. 2011), similar to the radiative effects responsible for shaping the spectral profile and escape of H I Lyα (e.g. Dijkstra & Kramer 2012; Verhamme et al. 2006; Laursen et al. 2009).

For Lyα it is now well established that emission is not confined to the ISM, but extends far out into the CGM. This halo-scale emission is not limited to the rare extreme Lyα halos around UV-bright quasars (e.g. Borisova et al. 2016), radio-loud AGNs, and Lyα blobs that are found in highly overdense regions and are likely powered by obscured AGNs (e.g. Steidel et al. 2000; Francis et al. 2001; Yang et al. 2009; Prescott et al. 2009, 2015; Cai et al. 2017). Extended emission is - at a weaker level - also typical around individual star forming galaxies (e.g. Steidel et al. 2011; Feldmeier et al. 2013; Momose et al. 2014; Wisotzki et al. 2016, 2018; Leclercq et al. 2017). Recent studies start to focus on spatially and kinematically resolving these typical Lyα nebulae (e.g. Erb et al. 2018; Claeyssens et al. 2019; Leclercq et al. 2020).

In extension of other similarities between Lyα and Mg II, one can expect that galaxies are also surrounded by Mg II emission halos. These would represent a reservoir of cool metal enriched gas, as revealed by the quasar absorption studies mentioned before. However, despite this expectation, there are only very few detections of extended Mg II CGM emission (Rubin et al. 2011; Martin et al. 2013), with also non-detections being reported (Rickards Vaught et al. 2019). This situation is about to change thanks to the tremendous efficiency gain provided by the current panoramic IFU spectrographs: MUSE /VLT and KCWI/Keck. In addition to increasing the number of objects with Mg II halo detections, these IFU data also allow for spatially resolved analysis of the extended emission with a level of detail not feasible based on slit spectroscopy. In a recent pioneering study, Burchett et al. (2021) performed such a detailed analysis, where they used the KCWI to re-observe a Mg II nebula around a starburst galaxy previously found by Rubin et al. (2011).

The MUSE GAs FLOw and Wind (MEGAFLOW) survey (paper I: Schroetter et al. 2016; paper II: Zabl et al. 2019; paper III: Schroetter et al. 2019; paper IV: Zabl et al. 2020; paper V: Wendt et al. 2021; paper VI: Schroetter et al. 2020, paper VII: Freundlich et al. 2021) is aimed at studying the properties of gas flows around star-forming galaxies with low-ionization absorption by Mg II ($\lambda\lambda$ 2796,2803) in 22 quasar fields. This survey, which combines VLT/UVES and VLT/MUSE observations, has enabled us to bring the sample size of galaxy-quasar pairs from a dozen (Bouché et al. 2012; Schroetter et al. 2015) to almost 80 pairs of which about 2/3 are suitable for studying outflows (Schroetter et al. 2019, hereafter, paper III). However, given that typical exposure times in the MEGAFLOW survey are 2–4hr, we acquired deeper MUSE observations with $>$ 10hr integration on two fields (SDSSJ0937+0656; SDSSJ0014−0028) in 2015-2018 with the aim to test whether the outflows detected in absorption against background quasars would be visible in emission with metal lines, such as Mg II. Here, we present the discovery of extended Mg II emission around a $z = 0.7$ galaxy in the field of SDSSJ0937+0656.

The paper is organised as follows. We present our observations in §2, the *main* galaxy and other objects in the field in §3, and our results for the CGM emission and absorption in §4 and §5, respectively. Then, in §6, we use a simple toy model to discuss the Mg II halo's properties. Finally, in §7, we conclude with a comparison to other objects. Throughout,

Table 1. Total exposure times and average seeing (Moffat FWHM at 7050 Å) split into observing nights. Only data with good quality that was used for the final cube are included. Also listed are the observing modes. NOAO and AO are short for WFM-NOAO-N or WFM-AO-N, respectively.

DATE-OBS	Mode	t_{exp} [hr]	Seeing $''$	Prog. ID.
2015-04-15	NOAO	1.00	0.55	095.A-0365(A)
2015-04-17	NOAO	1.00	0.90	095.A-0365(A)
2017-11-16	AO	0.28	0.55	0100.A-0089(B)
2018-02-14	AO	1.56	0.85	0100.A-0089(A)
2018-02-15	AO	3.11	0.70	0100.A-0089(A)
2018-03-18	AO	0.78	0.65	0100.A-0089(A)
2018-04-11	AO	1.56	0.59	0101.A-0287(A)
2018-04-14	AO	1.56	0.83	0101.A-0287(A)
2018-04-17	AO	0.39	0.80	0101.A-0287(A)

we use a 737 cosmology ($H_0 = 70\,\mathrm{km\ s^{-1}\,Mpc^{-1}}$, $\Omega_m = 0.3$, and $\Omega_\Lambda = 0.7$) and a Chabrier (2003) stellar Initial Mass Function (IMF). All distances are proper distances. All wavelengths and redshifts are in vacuum and are corrected to a heliocentric velocity standard. All fluxes are corrected for Galactic extinction (Schlegel et al. 1998). All stated errors are 1σ, unless otherwise noted.

2 OBSERVATIONS

The field centered on the $z = 1.82$ quasar SDSSJ0937+0656 was observed for a total of 13.6 hr with MUSE in 2015-2018. This on-source integration is slightly deeper than for the 3 $'\times3'$ mosaic MUSE observations in the UDF (Bacon et al. 2017) and allows us to reach a Mg II surface-brightness limit of $14.0 \times 10^{-19}\,\mathrm{erg\,s^{-1}\,cm^{-2}\,arcsec^{-2}}$ (2σ) (see §4.1).

The observations are described in Table 1. While the median seeing was $0''.8$, some observations were rejected due to either technical issues or poor seeing (FWHM$>1''.0$). The total usable science exposure is 11.2 hr. We created our main cube from this dataset. In addition to this full set of usable exposures, we also selected a sub-set including only the 3.36 hr with the best image quality (FWHM $< 0''.6$), in order to better constrain morphology and spatial variations of the foreground galaxy's line fluxes.

We reduced the data similarly as in papers II–IV, but using the newer Data Reduction Software (DRS) v$\geq$ 2.4 (Weilbacher et al. 2016, 2020) which includes the auto-calibration of the fluxes in the slices (e.g. Bacon et al. 2015, 2017). Compared to our initial data reduction, where we masked regions with strong flat-fielding imperfections at the edges of slices, here we used the method advocated by Bacon et al. (2021) to improve the flat-fielding through applying a 'super sky-flat'. This consists of median combining all the sky-subtracted exposures (masking the sources) to produce a sky-flat, which can then be subtracted from the individual exposures. We create this master flat from the pixtables rather than the cubes to enhance computation efficiency[1], and refer to this sky-flat in the following as 'super-fast super-flat' (SF^2).

In practice, we used here a SF^2 constructed from 36 exposures from another MUSE GTO program (the MUSE eXtreme Deep Field [MXDF]; PI: Bacon) taken during observing runs overlapping with our observations (in August 2018). After testing, we applied this SF^2 to our AO (adaptive optics) data taken from Nov 2017 to April 2018 as it does not only improve the flat-fielding at the slice edges, but also reduces sky-line residuals. For the non-AO exposures, we applied simpler masks, as in papers II–IV. Further details about the new reduction chain will be given in the survey paper (Bouché et al. in prep.).

As part of the MEGAFLOW survey, we also observed the quasar SDSSJ0937+0656 with the VLT high-resolution spectrograph UVES (Ultraviolet and Visual Echelle Spectrograph; Dekker et al. 2000) for a total integration time of 9 ks in the nights of 2015-12-20 and 2016-01-11. Further details about the observation, reduction, and continuum normalisation can be found in paper II.

3 THE OBJECT

The quasar SDSSJ0937+0656 sightline has three strong Mg II absorbers at redshifts of 0.702, 0.857, 0.933 with rest-frame equivalent widths $EW_0^{\lambda2796} = 1.8$, 1.0 and 1.5 Å, respectively. In all three cases we have been able to identify at least one galaxy associated with the absorber within 100 kpc of the quasar. The galaxies associated with the $z = 0.702$ and $z = 0.933$ absorbers were first discussed in paper III. The galaxy associated with the $z = 0.857$ absorber was not included in the previous MEGAFLOW papers due to its low [O II] flux.

In the present paper, we focus on the absorber at $z = 0.702$, for two reasons: first, because it has the lowest possible Mg II redshift within the MUSE wavelength coverage, it favors our ability to detect low surface brightness emission. Second, because this absorber has (at least) one galaxy whose position angle (PA) is such that the quasar is approximately along the galaxy projected minor axis, which favors, as motivated in the introduction, outflows causing Mg II absorption. As discussed in paper III, this $z = 0.702$ absorber actually has two galaxies at the redshift of the absorber within 100 kpc of the quasar.[2] In addition, we searched for a putative fainter companion located under the quasar PSF and found no evidence for such a companion to a flux limit 10× fainter than the *main* galaxy. The quasar PSF can be well subtracted around the observed wavelength of the [O II] doublet (6343 Å). By placing the *main* galaxy at the quasar location and rescaling its flux by 1/5 or 1/10, such companion would have been detected in both cases.

The *main* galaxy is at an impact parameter $b_1 = 38.7\,\mathrm{kpc}(\approx 0.2\,r_{vir})$, while the *secondary* galaxy's impact parameter is approximately twice as large with $b_2 = 69.0\,\mathrm{kpc}(\approx$

[1] Alternatively, each of the typically 30 frames used in a master flat must be resampled 30 times to put each of them on the same WCS grid.

[2] For completeness, in addition to these two galaxies within 100 kpc of the quasar, we have identified within a search window of $\pm400\,\mathrm{km\ s^{-1}}$ around the absorber redshift two further galaxies at 224 and 245 kpc, respectively. In addition to their much larger impact parameter, these are also >10 times fainter than the *main* galaxy.

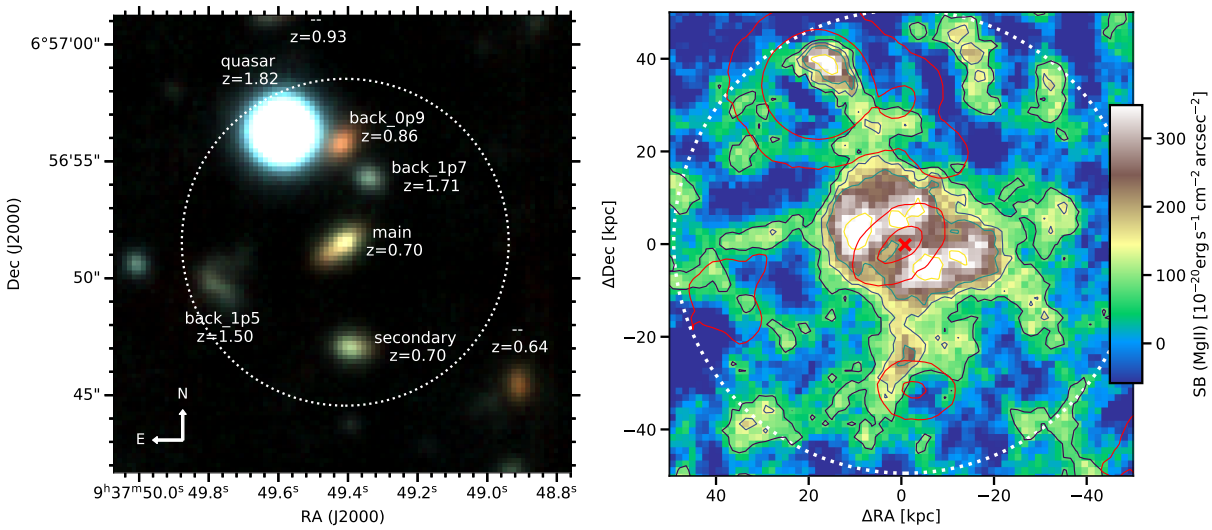

Figure 1. Left: 20 arcsec × 20 arcsec field around the *main* galaxy with (pseudo-) i', r', and V filters in the red, green, and blue channels of the colour image, respectively. The surrounding galaxies are labelled and the redshifts are stated (see also Table 3 and §5.3). The dotted white ring is centred on the *main* galaxy and has a radius of 50 kpc at $z = 0.7021$. The centre, which is used throughout the paper, was determined from a GALFIT fit to a pseudo r' image (see Fig. A3). **Right:** SB emission map created with a 600 km s^{-1} double NB filter (see Fig. 2). The map was smoothed with a tophat filter with a diameter of 10 kpc (1.4″). The dotted white ring has an identical radius as the colour image in the left panel. The black, grey, green, and yellow contours correspond to surface brightness levels of 7, 14, 21 and 35×10^{-19} erg s^{-1} cm^{-2} arcsec^{-2} (1, 2, 3, and 5σ). For the Mg II SB map all (projected-) neighbours, including the quasar, have been subtracted in the cube (see text §4.1). The red contours (23.9 and 26.2 mag arcsec^{-2}; arbitrarily chosen) are for a MUSE white-light continuum image convolved with the same kernel as the SB image. These contours show both the position of the *main* galaxy and those of the neighbours (c.f. left). The continuum peak of the *main* galaxy is indicated as red cross.

0.6 $r_{\rm vir}$), or even three times as large when normalized with the respective galaxy's virial radius. Fig. 1 (left) shows the location of the *main* and *secondary* galaxies in relation to the quasar location and three background galaxies, back_1p7 at $z = 1.71$, back_1p5 at $z = 1.50$, and back_0p9 at $z = 0.86$. Two further background galaxies within 50 kpc of the *main* galaxy are too faint to be visible in Fig. 1 (left), and we will not discuss them further.[3]

Using the azimuthal angle α, defined as the projected angle between the galaxy's major axis and the apparent quasar location (see Fig. 1 of paper II), the sightline is suitable as a 'wind' probe for both *main* and *secondary* galaxies, as the azimuthal angle is 87 ± 1 deg (58 ± 1 deg) for the *main* (*secondary*) galaxy. But, given the strong anti-correlation between $EW_0^{\lambda 2796}$ and b (e.g. Lanzetta & Bowen 1990; Chen et al. 2010; Nielsen et al. 2013), we will assume that the majority of the Mg II absorption is caused by gas flows associated with the closest of the two galaxies, *main* ($b_1 = 38.7$ kpc). The much lower M_* and SFR of the *secondary* galaxy, which has less than 1/5 of the *main* galaxy's M_* and about half its SFR, makes it a minor companion, which gives further credibility to associating the absorption primarily with the *main* galaxy.

As discussed in paper III, the *main* galaxy is a main-sequence galaxy which has a SFR of $10 - 20$ M$_\odot$ yr^{-1} and a stellar mass of $\log M_\star/{\rm M}_\odot \simeq 10.5$, which was estimated in paper III from the Tully-Fisher like scaling relation between $S05$ ($\equiv \sqrt{0.5\, v_{\rm max}^2 + \sigma_0^2}$) and stellar mass (e.g. Kassin et al. 2007). In addition, paper VII recently constrained the SFR of this galaxy using dust continuum observations to $< 23.8\,{\rm M}_\odot\,{\rm yr}^{-1}$ ($3\,\sigma$), ruling out a dust-obscured starburst. Here, we perform a spectral energy distribution (SED) fit directly to our MUSE data and found that $\log M_\star/{\rm M}_\odot = 10.05^{+0.15}_{-0.11}$ using our custom code CONIECTO (as in paper II, paper IV, and Zabl et al. 2016). Using strong-line calibrations from Maiolino et al. (2008) we infer for the *main* galaxy a gas-phase metallicity of about solar, which is a typical value for its mass and redshift. Further details about stellar mass and metallicity can be found in Appendix A1 and A4, respectively.

Perhaps the most relevant galaxy property for this paper is the galaxy's inclination. However, we find that the *main* galaxy contains a significant clump of SFR offset from the kinematic centre (see Appendix A2) which impacts the morphology and the determination of the inclination i from [O II]. In addition, as we will show in §4.2, the [O II] flux map contains extended emission (towards the minor axis), which will bias the determination of i. Thus, the most reliable estimate of the inclination (and PA) of the *main* galaxy can only be obtained from fitting a model to the continuum.

Using a pseudo-broadband image for the r' passband, the best-fit flux model obtained with GALFIT (Peng et al. 2010) (see Appendix A2 for further details) has a Sérsic index of 0.50, half-light radius $R_{\rm e} = 4.6 \pm 0.1$ kpc, and an inclination of $i = 75.7$ deg, using a Moffat PSF with the parameters as measured from the quasar. We will adopt this inclination, $i \simeq 75$ deg for the rest of this work.

We measure the kinematics of the *main* galaxy using CAMEL (Epinat et al. 2012) and GALPAK$^{\rm 3D}$ (Bouché et al.

[3] A $z = 1.06$ galaxy (09:37:49.67 +06:56:54.2) is close to the quasar and a $z = 1.27$ galaxy (09:37:49.69 +06:56:51.0) is in close proximity of the back_1p5 galaxy.

Table 2. Physical properties of the *main* galaxy associated with the $z = 0.70$ absorber. For further details, see paper II. (1) [O II] flux; (2) nebular extinction from E(B–V) – M_* relation; (3) nebular extinction from SED fit; (4) instantaneous SFR from [O II] assuming E(B-V) from (2); (5) instantaneous SFR from (3; SED fit); (6) stellar mass from SED fit; (7) rest-frame B absolute magnitude from best-fit SED model; (8) distance from the main-sequence of star-forming galaxies (assuming main-sequence from Boogaard et al. 2018); (9) age of galaxy from SED fit (time since onset of star-formation); (10) decay time in delayed τ SFH from SED fit; (11) half-light radius R_e from GALFIT continuum fit; (12) rotation velocity from GALPAK^{3D} fit; (13) velocity dispersion from GALPAK^{3D} fit; (14) adopted inclination i (deg); (15) virial velocity; (16) virial radius from v_{vir}; (17) virial mass from v_{vir}; (18) redshift from [O II].

Row	Property	*main*	Unit
(1)	$f_{[O II]}$	$19.6^{+0.1}_{-0.1} \times 10^{-17}$	erg s^{-1} cm^{-2}
(2)	E(B-V) (M_*)	$0.29^{+0.10}_{-0.09}$	mag
(3)	E(B-V) (SED)	$0.42^{+0.05}_{-0.26}$	mag
(4)	SFR ($f_{[O II]}$)	9^{+4}_{-4}	M$_\odot$ yr^{-1}
(5)	SFR (SED)	$22.8^{+15.4}_{-19.0}$	M$_\odot$ yr^{-1}
(6)	M_* (SED)	$10.05^{+0.15}_{-0.11}$	log(M$_\odot$)
(7)	B	-20.4	mag
(8)	$\delta(MS)$	$0.4^{+0.3}_{-0.5}$	dex
(9)	age	$8.4^{+0.7}_{-0.0}$	log(yr)
(10)	τ	$7.9^{+1.9}_{-0.0}$	log(yr)
(11)	R_e	4.6 ± 0.1	kpc
(12)	v_{max}	190^{+8}_{-8}	km s^{-1}
(13)	σ_0	57^{+1}_{-1}	km s^{-1}
(14)	i	75.7	deg
(15)	v_{vir}	180^{+14}_{-14}	km s^{-1}
(16)	r_{vir}	208^{+16}_{-16}	kpc
(17)	M_{vir} (from kin.)	$12.19^{+0.09}_{-0.09}$	log(M$_\odot$)
(18)	z	0.7021 ± 0.0001	

2015) as described in Appendix A3 and find that the maximum velocity is $V_{max} = 190^{+8}_{-8}$ km s^{-1}, and the disk dispersion is $\sigma_0 = 57^{+1}_{-1}$ km s^{-1}. These parameters were inferred using a fixed inclination (75.7 deg) and a deconvolved [O II] flux model that we obtained with GALFIT.[4] The estimated virial velocity and halo mass from the kinematics are $v_{vir} = 180^{+14}_{-14}$ km s^{-1} and $\log M_h/M_\odot = 12.19^{+0.09}_{-0.09}$, respectively. For the galaxy's redshift we find both from the kinematic fitting and from visual inspection of a position-velocity-diagram a best fit redshift of $z = 0.7021$. We estimate the uncertainty of the [O II] redshift to be about 20 km s^{-1}.

Table 2 lists all properties of the *main* galaxy associated with the $z = 0.702$ absorber. Coordinates of both the *main* and the *secondary* galaxy are listed in Table 3.

4 HALO IN EMISSION

The main purpose of the present study is to use our MEGAFLOW-deep MUSE cube (11.2 hr) to test whether we can detect the circumgalactic Mg II in *emission* around galaxies with known Mg II *absorption* in transverse quasar sightlines. We focus here on the most promising candidate, which is the *main* galaxy (see §3) associated with the strong $z = 0.70$ Mg II absorber. We defer a statistical analysis of the presence or absence of Mg II emission halos in the full MEGAFLOW sample to a later paper. We note that we do not detect extended Mg II emission around the galaxies that are associated to the other two absorbers ($z = 0.86$ and 0.93) in the SDSSJ0937+0656 sightline.

4.1 Mg II emission map

We searched for extended Mg II emission around the *main* galaxy by creating a double pseudo-narrowband filter centred on the expected observed frame wavelength of Mg II. The transmittance curve of this double filter was centred on the 2796 and 2803 lines of the Mg II doublet, respectively. Each of the two passbands was chosen to be 600 km s^{-1} wide.[5] After converting to units of surface-brightness, we refer to this narrowband (NB) image in the following as the Mg II surface-brightness map (SB-map).

We subtracted the continuum to first order by taking the median in the spectral direction in a $\pm$10000 km s^{-1} window around Mg II.[6] For non-resonant lines, such as e.g. [O II], this standard approach of continuum subtraction is usually sufficient to remove the continuum of both the targeted galaxy and other galaxies in the field. However, for resonant lines, such as Mg II, the same gas that we aim to probe in emission will also imprint itself as absorption on the background sources. This absorption will show up in an off-band subtracted NB image (or cube) as negative flux. To mitigate this effect, we subtracted the background sources from the layers that contribute to the NB images using a 3D model.

For subtracting the quasar (including the Mg II absorption), we tested both using an empirical, non-parametric, PSF model and a wavelength-dependent parametric model. In the latter case, we determined the best-fit Moffat PSF parameters (Moffat 1969) as a function of wavelength using the PAMPELMUSE code (Kamann et al. 2013). The fitted FWHM varies monotonically from 0.81″ in the blue (4750 Å) to 0.56″ in the red (9300 Å) which will be used for the morphology and kinematics analysis of the *main* galaxy. While overall a good representation of the PSF, this Moffat model leaves residuals for the relatively bright quasar that can impact Mg II emission measurements around the *main* galaxy. Therefore, for the quasar subtraction over the wavelength range relevant for the NB filter, we constructed an empirical PSF from an image with a relatively large velocity range ($\pm$10000 km s^{-1}) around the considered line, excluding the line itself. To further increase the signal in the outer part of this empirical PSF image and to avoid being impacted by neighbouring sources, we replaced the empirical PSF in the outer part ($> 1.4''$ away from the quasar) with the median flux in annuli.

Similarly, for subtracting the relevant background galaxies (back_1p7, back_1p5, back_0p9) and the *secondary* galaxy, we first created a model with GALFIT using an r'

[4] We expect systematics of about 5–10 deg (see, e.g., Appendix A of paper II) to dominate uncertainties on the i.

[5] The separation of the two lines is 770 km s^{-1}. This means that the filter has a gap of 170 km s^{-1}.

[6] To the blue of Mg II, not the full 10000 km s^{-1} was available.

Table 3. Information about position and orientation of the *secondary* galaxy and the four background sightlines w.r.t. the *main* galaxy, including impact parameter, b, azimuthal angle, α ($0\,\mathrm{deg} \leq \alpha \leq 90\,\mathrm{deg}$), redshift, and observed magnitude at the wavelength corresponding to Mg II at the redshift of the *main* galaxy.

Name	[unit]	main	*secondary*	quasar	back_1p5	back_0p9	back_1p7
R.A. (J2000)	hms	09:37:49.42	09:37:49.38	09:37:49.59	09:37:49.77	09:37:49.42	09:37:49.34
Dec (J2000)	dms	+06:56:51.5	+06:56:47.1	+06:56:56.3	+06:56:49.6	+06:56:55.8	+06:56:54.3
b (from *main*)	kpc	–	32	39	40	31	22
α (from *main*)	deg	–	60	82	17	56	32
redshift (of background galaxy)		0.702	0.702	1.82	1.495	0.857	1.713
m @ 4760 Å	mag	23.5	23.8	19.4	24.3	24.8	24.1

(pseudo-)broadband image created from the MUSE cube and fit this model to each layer of the cube taking into account the appropriate PSF. The fitting was done in a conceptually identical way to that used in codes such as PAMPELMUSE (Kamann et al. 2013) or TDOSE (Schmidt et al. 2019). Subsequently, we removed the best fit from each layer. These layer-by-layer fits also provide optimally extracted spectra.

The resulting Mg II SB-map is shown in Fig. 1 (right). We smoothed it with a tophat with a diameter of 1.4″ (10 kpc at $z = 0.70$). Contours corresponding to the five (yellow), three (green), two (grey), and one (black) sigma significance levels of the smoothed map are shown on the map. These significance levels correspond to surface-brightnesses of 35, 21, 14, and $7 \times 10^{-19}\,\mathrm{erg\,s^{-1}\,cm^{-2}\,arcsec^{-2}}$, respectively.[7] The significance levels were determined based on the standard deviation of 80 independent pixels in object-free regions over the full MUSE FOV that were far enough apart from each other not to be correlated after smoothing. Also shown (in red) are the contours of the white light-image with the same smoothing applied.

In Fig. 2, we show the Mg II spectrum of the full halo. This spectrum was extracted from the $2\,\sigma$ contour of the Mg II SB map (grey contour in right panel of Fig. 1). The blue vertical bands in Fig. 2 indicate the passband of the double NB filter used to create the SB map in Fig. 1 (right). This passband encompasses the majority of the Mg II flux and is hence a well motivated choice. While it misses some flux at higher velocities, we show in Appendix B that this extra flux does not change the morphology of the halo. The total Mg II flux (2796+2803) within the blue ($\pm 300\,\mathrm{km\,s^{-1}}$) passband is $41 \pm 3 \times 10^{-18}\,\mathrm{erg\,s^{-1}\,cm^{-2}}$, with a 2796/2803 ratio of 1.9 ± 0.3. This ratio agrees with the value of 2.0 expected for optically thin emission. The flux corresponds to a luminosity of $9.0 \pm 0.7 \times 10^{40}\,\mathrm{erg\,s^{-1}}$.

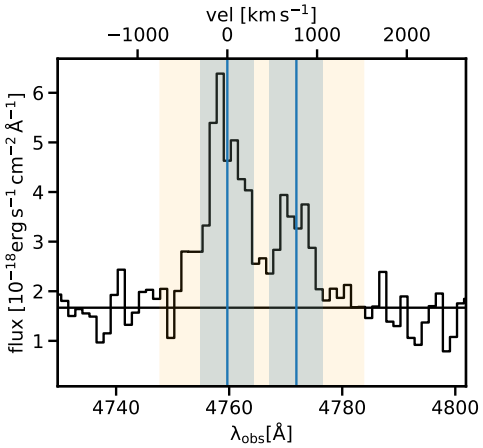

Figure 2. Spectrum around the observed wavelength of the Mg II doublet extracted from a large spatial aperture corresponding to the 2σ contour in Fig. 1 (right). The black horizontal line indicates the local continuum level estimated by excluding the wavelength range covered by the yellow region. The blue shaded regions indicate the width ($600\,\mathrm{km\,s^{-1}}$ each) of the double NB filter used for creating the SB map in Fig. 1. By contrast, the yellow shaded region extents continuously over the full range from $-750\,\mathrm{km\,s^{-1}}$ bluewards of the 2796 line to $750\,\mathrm{km\,s^{-1}}$ redwards of the 2803 line. A SB map using this more inclusive filter is discussed in Appendix B.

4.2 Morphology of the Mg II halo

Fig. 1 (right) shows that the Mg II emission extends out to at least 20 kpc from the galaxy. Above the 2σ SB threshold of $14.0 \times 10^{-19}\,\mathrm{erg\,s^{-1}\,cm^{-2}\,arcsec^{-2}}$ it encompasses an area of $19\,\mathrm{arcsec^2}$, corresponding to $9.8 \times 10^2\,\mathrm{kpc^2}$. The morphology of the Mg II emission is very different from that of the continuum. The strongest Mg II emission appears along the minor axis of the galaxy.

In order to analyze the morphology of the Mg II emission, we show in Fig. 3 the radial surface brightness profile extracted along the minor and major axes of the *main* galaxy respectively. The Mg II profile along the minor axis is relatively flat out to about 20 kpc, after which it drops significantly. While not extending as far out along the major axis, the profile is still substantially flatter than the continuum and even increasing in the inner part.

One complication is that the lack of positive flux at the position of the central galaxy might not be an actual lack of emission, but can be caused by Mg II absorption in the galaxy's down-the-barrel spectrum. Indeed, Mg II spectra centred on galaxies often show absorption, with part of the absorption infilled by redshifted emission (P-Cygni like profiles; e.g., Weiner et al. 2009; Martin & Bouché 2009; Erb et al. 2012; Finley et al. 2017b; Feltre et al. 2018). In order to recover the full emission, one can attempt to simultaneously fit emission and absorption (e.g. Martin et al. 2012).

Fig. 4 (black curve) shows the central Mg II spectrum of the *main* galaxy extracted from an elliptical aperture with a semi-major axis of 1″. While no strong absorption and little emission is directly visible in this spectrum, it is still possible that emission and absorption almost exactly can-

[7] Values are the average SB within the spatial smoothing filter, which has an area of $1.5\,\mathrm{arcsec^2}$.

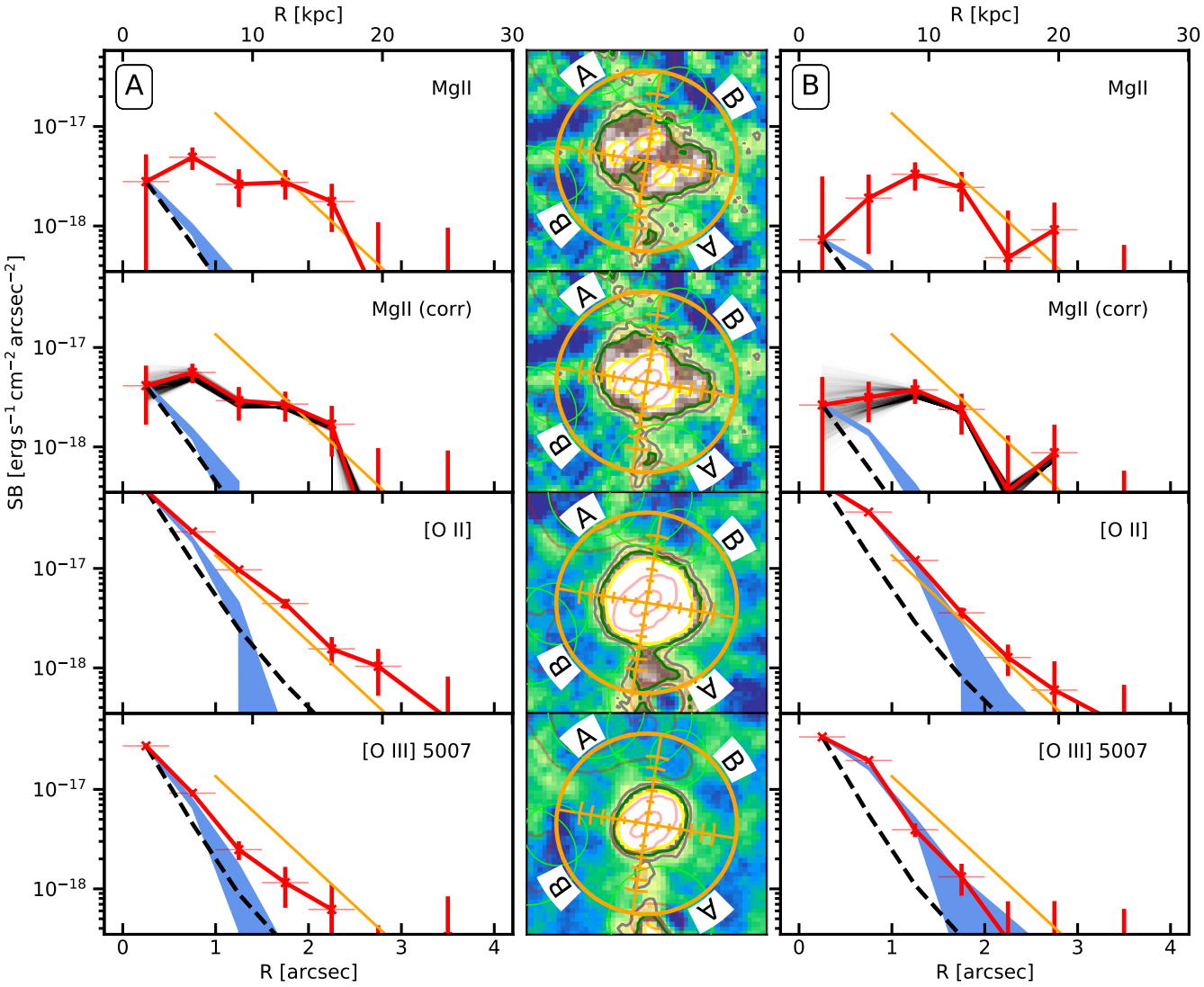

Figure 3. Radial surface brightness profiles (median) are shown for Mg II (1st row), [O II] (3rd row), and [O III] λ5007 (4th row) along both the minor (left, A) and major axis (right, B) of the *main* galaxy. The red solid curves show the respective emission line surface brightness (SB). The black dashed line shows the PSF profile as determined from the quasar and the blue curve is the profile of the galaxy's continuum. The arbitrary orange exponential profile is identical in all six panels and is meant as a visual aid for comparison of the different profiles. The respective cone-like regions used for the minor and major axis profiles are indicated (orange) in the line SB maps (middle column). The radial bin edges are indicated by little fins, with the first bin starting in the centre. All radial bins have a width of 0″.5, except the outermost, which has double the width. The outer edge of this last bin is the full circle, which is at a radius of 4″ (= 28.6kpc) For comparability, the [O II] and [O III] SB maps were determined with the same filter width as that used for Mg II (600km s^{-1}; for [O II] extended by 224km s^{-1} to take account for the doublet). Regions potentially contaminated by residuals from neighbouring galaxies have been excluded from the profile extraction both for the line and continuum profiles, and are indicated as green ellipses. The errors for both the line (red vertical bars) and the continuum (extent of blue shading) have been determined based on empty apertures (see text in §4.2) and are 2σ. The thin red horizontal bars indicate the radial bins. Both PSF and continuum profiles have been determined from a ±10000 km s^{-1} wide window around the respective emission line, excluding the emission itself. Further, these two curves have been arbitrarily scaled to match the line surface brightness profile in the innermost bin. Finally, a version of the Mg II profile after correcting for likely weak continuum absorption is shown in the 2nd row. The grey curves are based on random realizations of absorption profiles taken from the MCMC chain obtained, and indicate the uncertainty of this correction (see §4.2).

cel. To investigate this possibility, we performed a formal decomposition using a model and an MCMC algorithm as described in Wisotzki et al. in prep. For details about the code we refer the reader to this publication, but in short: The model assumes Gaussians for both the optical depth distribution of the absorption and for the flux distribution of the emission. The velocity offsets and widths of these Gaussians are free parameters and are independent between absorption and emission, but were assumed to be identical for the 2796 and 2803 lines in both cases. The optical depth ratio between

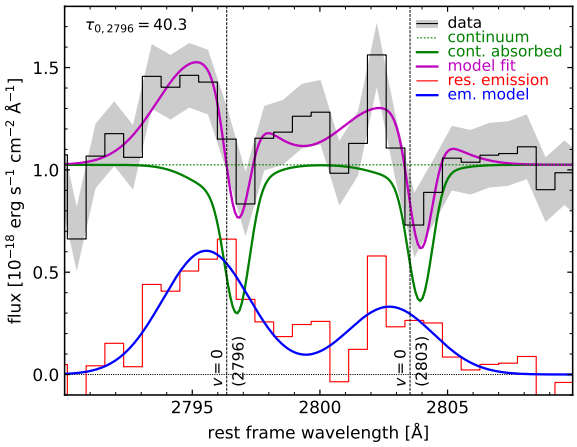

Figure 4. Decomposition of the *main* galaxy's Mg II spectrum into absorption and emission. The observed spectrum (black steps with grey errorband) was extracted from an elliptical aperture with a semi-major axis of 1″. The purple line is the best-fit model, which is a linear combination of a continuum with doublet absorption (green solid line) and doublet emission (blue solid line). A direct subtraction of the absorption spectrum from the observed spectrum (red steps) is as expected consistent with the emission model. The observed wavelengths of Mg II λ2796 and 2803 at the systemic redshift of the *main* galaxy are indicated by vertical lines. Further details are given in §4.2.

the 2796 and 2803 absorption was fixed to 2:1 and unit covering was assumed. The flux ratio between the two emission lines was a free parameter within the 2796/2803 range from 0.1 to 2.5. Finally, the model was convolved with the spectral resolution of the MUSE data.

Fig. 4 (purple line) shows the resulting best fit.[8] This best-fit model describes the data very well and is a superposition of the (green) model absorption spectrum and the (blue) model emission spectrum. This means that the actual Mg II emission from within the elliptical aperture is likely a factor of about 2 higher than what one would measure from a simple NB image.

In Fig. 3 (second row), we show the impact of this correction on the SB emission map (created as in §4.1). The full, corrected emission is estimated by rescaling the offband continuum cube by the absorption spectrum, as inferred from the decomposition fit described above, before subtracting it from the cube. An implicit assumption in this process is that the normalized absorption profile is identical over the galaxy's full extent. As expected, the correction mainly removes the central flux suppression. However, the radial profile still remains relatively flat without a central peak.

4.3 Kinematics of the Mg II halo

While the SB map is illustrative (shown in Fig. 1 right), the MUSE data cube allows to go further and analyse the spatial variations of the Mg II kinematics and spectral shape. Fig. 5 shows the Mg II spectra extracted in different regions. The red spectra in the left and right bottom panels of Fig. 5

[8] Best fit means here a model with parameters corresponding to the 50% percentile in the marginalized 1D distributions.

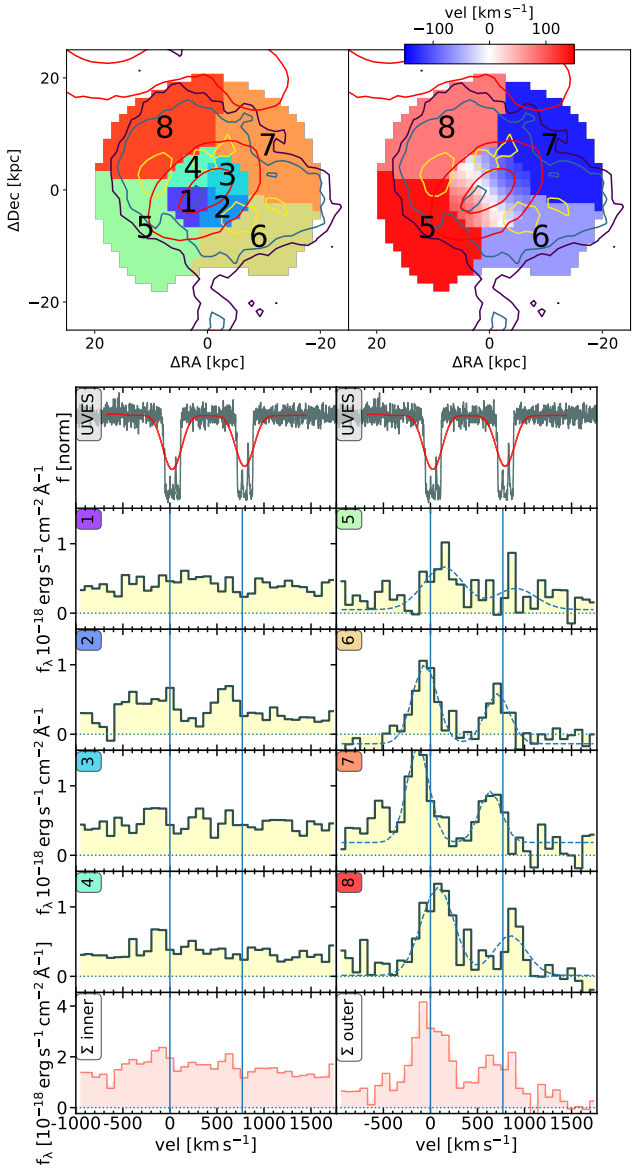

Figure 5. Spatial variations of the Mg II emission spectrum. We extracted spectra in 8 different regions, as defined in the map on the top-left. The color-coding in the top-left panel is arbitrary. The respective extracted spectra, are shown in yellow below. Regions 1 to 4 (left column) extend out to a radius $r \leq 1''$ (7.2 kpc), while regions 5 to 8 (right column) cover the radial range $1'' < r \leq 2.8''$(7.2–20 kpc). The odd numbered regions are along the *main* galaxy's major axis, while the even numbered regions are along the minor axis. The two red spectra in the bottom row correspond to the sum of the four yellow spectra in the corresponding columns. This is identical to an extraction from an inner aperture (left) and an outer annulus (right), respectively. The two panels in the top row are identical and show the UVES quasar spectrum at the wavelength corresponding to Mg II at the redshift of the *main* galaxy (see §5.1). The UVES spectrum (grey) is also shown convolved with the resolution of MUSE (red). The velocity scale of the spectra is for Mg II 2796 and is w.r.t. the systemic redshift of the galaxy. The two blue vertical lines indicate the observed wavelengths of the 2796 and 2803 lines at this systemic redshift, respectively. Gaussian doublet fits are shown for the four outer regions as blue dashed line. The velocities obtained from these fits are shown in the upper-right map, where for comparison also the galaxy velocity field as measured from [O II] with GALPAK^{3D} is shown.

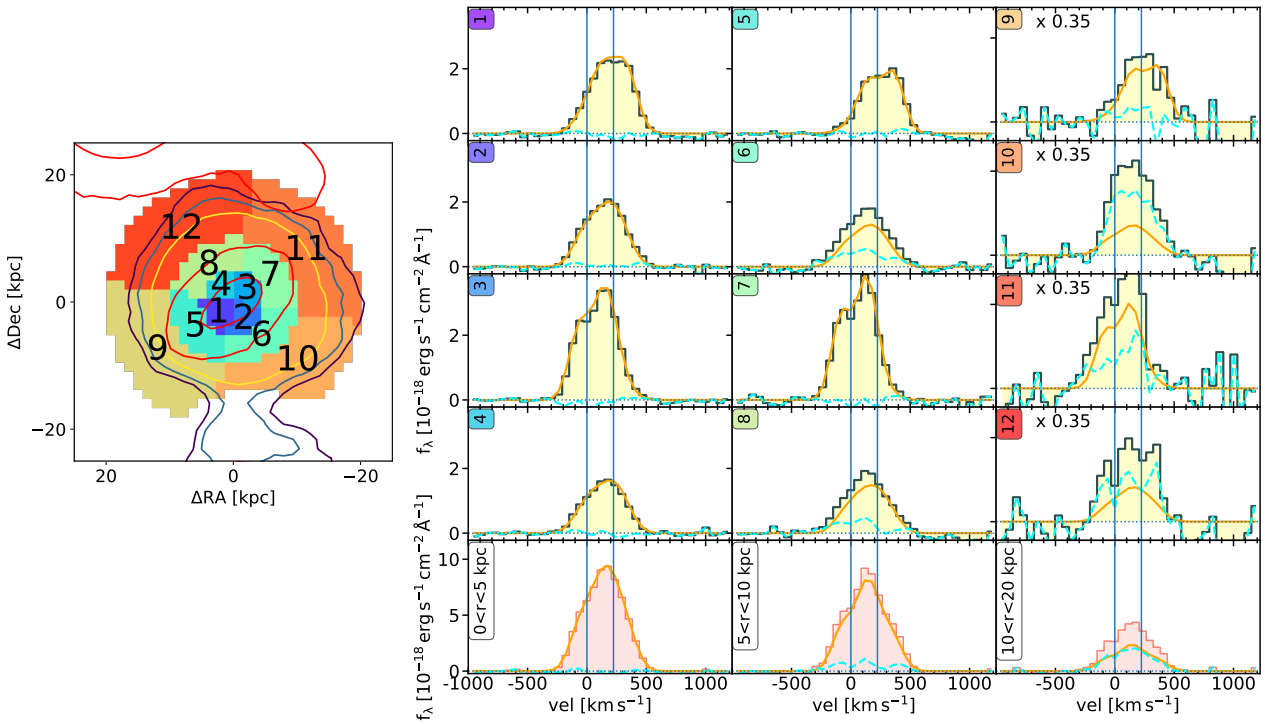

Figure 6. [O II] spectra from multiple spatial regions around the *main* galaxy. Spectral extractions for the 12 numbered regions indicated in the map (left) are shown on the right (black line and yellow shading). A region around the neighbouring *secondary* galaxy has been excluded to mostly avoid contribution from residual [O II] emission of this galaxy, which reduces the size of regions 9 and 10 slightly compared to regions 11 and 12. The velocity scale is for [O II] 3727 and is w.r.t. the systemic redshift of the galaxy. The two blue vertical lines indicate the observed wavelengths of the 3727 and 3729 lines at this systemic redshift, respectively. The y-scale for the spectra of regions 9–12 has been reduced by a factor 0.35 compared to that used in regions 1–8. The sum of the spectra from the four inner regions (regions 1–4; $r < 5$ kpc (0.7″)), the four middle regions (regions 5–8; 5 kpc (0.7″) $< r <$ 10 kpc (1.4″)), and the four outer regions (regions 9–12; 10 kpc (1.4″) $< r <$ 20 kpc (2.8″)) are in the bottom row. The orange solid lines are spectra extracted from the best-fit GALPAK^{3D} model cube (see §3) in an identical way as from the data. The cyan dashed line is the residual after subtracting the GALPAK^{3D} model from the data and can be interpreted as excess flux above the ISM emission.

are spectra extracted in annuli with a radial range of 0–1″ (0.0–7.2 kpc) and 1–2.8″ (7.2–20 kpc).

Going one step beyond simple annuli, we split the two annuli into four quadrants each (Regions 1–8 of Fig. 5). The four regions comprising the inner annulus (1–4), which cover the ISM of the *main* galaxy rather than its CGM, show very little Mg II emission individually. The outer regions 5 and especially 7 (along the *main* galaxy's major axis) appear to have less Mg II emission than the outer regions 6 and 8 (along the minor axis), consistent with the visual impression from Fig. 1 (right).

Interestingly, the south-east region (5) is redshifted w.r.t. the *main* galaxy's systemic redshift (+139 km s^{-1})[9], while the north-west region (7) is blueshifted (−132 km s^{-1}), consistent with an extension of ISM rotation field (see velocity coded region map in Fig. 5). This could indicate that the Mg II emission seen along the major axis traces the co-rotating extended gaseous disks that have been seen so far in absorption (e.g. Bouché et al. 2016; Ho et al. 2017; paper II).

Furthermore, Fig. 5 also reveals that the two regions along the minor axis (6 and 8) have a clear velocity shift with respect to each other. The region towards the south-west (6) is blue-shifted (−59 km s^{-1}) and the opposite region (8) is red-shifted (+78 km s^{-1}). Given that these two regions are approximately coincident with the two bipolar peaks seen in the Mg II emission map (Fig. 1 right), this provides us with crucial kinematic information to characterize a putative bi-conical outflow (see also §6.1). In Appendix C, we rule out that the kinematics in these two regions might be caused by a combination of rotation and the observed slightly inhomogenous flux distribution.

In summary, the Mg II emission appears to have complex, but coherent kinematics connected to both the disk kinematics along the major-axis and to the outflow kinematics along the minor-axis. Therefore, the line shape of a spectrum obtained by summing over the full halo (Fig. 2) or over annuli (Fig. 5; bottom row) might be shaped more by a superposition of different kinematic components than by radiative effects. In §6, we discuss a possible explanation for the coherent motions.

4.4 Halo emission from other lines

For comparison, we also show the [O II] and [O III] profiles in Fig. 3. The profiles along the major axis are mostly consistent with the slope of the continuum profile. Along the minor axis, however, the [O II] emission is significantly more extended and the [O III] emission potentially slightly more

[9] Best-fit value from Gaussian doublet fit.

extended than the continuum. The observed [O II]/Mg II ratio[10] decreases along the minor axis from 20 in the central $0''.5$ to $\approx$ 1–2 at $2'' \pm 0.5$. Even when correcting for potential down-the-barrel Mg II absorption in the centre (see §4.2), the ratio changes still by an order of magnitude between the centre ([O II]/Mg II = 10) and the outer parts. The [O III]/[O II] ratio seems to decrease over the same range from 1/2 in the centre to $\approx 1/3$ at $2''$.

For [O II], we performed a spatially resolved kinematics analysis in multiple regions along the minor and major axes, similar to what we did for Mg II in Fig. 5. Given the more centrally peaked radial SB of [O II] compared to Mg II, we decided to put the regions at different radii than in the case of Mg II ($r \leq 5\,\mathrm{kpc}$, $5\,\mathrm{kpc} < r < 10\,\mathrm{kpc}$, and $10\,\mathrm{kpc} < r < 20\,\mathrm{kpc}$). Spectra for the twelve regions defined in the left panel of Fig. 6 are shown in the right of the same figure (black line/solid yellow shading). It is very revealing to compare each of these spectra to spectra obtained in an identical way from the best-fit GALPAK^{3D} [O II] model (see §3). The difference between these model spectra (orange) and the data allows us to assess excess halo emission (cyan). Little excess flux is needed in the regions along the major axis even at large radii. Except in the region 11, the excess flux is essentially zero, and even in region 11 the excess flux is subdominant. By contrast, already in the radial range from $5\,\mathrm{kpc} < r < 10\,\mathrm{kpc}$ significant excess flux is needed for the two minor axis regions (regions 6 and 8). The excess flux dominates in the two outer minor axis regions. The total [O II] excess flux out to 20 kpc is $26 \pm 2 \times 10^{-18} \mathrm{erg\,s^{-1}\,cm^{-2}}$. For comparison, the total Mg II flux (2796+2803) out to 20 kpc is $39 \pm 5 \times 10^{-18} \mathrm{erg\,s^{-1}\,cm^{-2}}$. Making the assumption that all Mg II flux but only the excess portion of the [O II] flux are produced outside the ISM, this implies a Mg II/[O II] ratio larger than one in the CGM.

While it is difficult to interpret the kinematics of the excess flux due to the unknown doublet ratio and the low signal-to-noise (S/N), the kinematics appear consistent with that seen in Mg II along the minor axis. This is a relatively small velocity shift compared to systemic. The comparison between the Mg II halo morpho-kinematics and the morpho-kinematics of the [O II] halo excess flux is very suggestive of a similar spatial distribution of the [O II] emitting and the Mg II emitting/scattering gas.

5 HALO IN ABSORPTION

While Mg II emission maps provide a novel way to *image* the cool metal-enriched CGM, as in, e.g. Rubin et al. (2011); Martin et al. (2013); Burchett et al. (2021), Wisotzki et al. (in prep), Leclercq et al. (in prep), the total luminosity of the halo has a natural limit in the number of photons injected by the central galaxy that are in resonance with Mg II ions in the CGM. By contrast, the absorption that the gas imprints on the spectra of background sightlines is independent of the brightness of the central source, and solely depends on the column density along the line-of-sight.

[10] We determined the flux ratios using maps with their PSF matched to the map with the lowest resolution (Mg II). In practice, we determined the matching kernels empirically using Gaussians modified by polynomials (Alard & Lupton 1998).

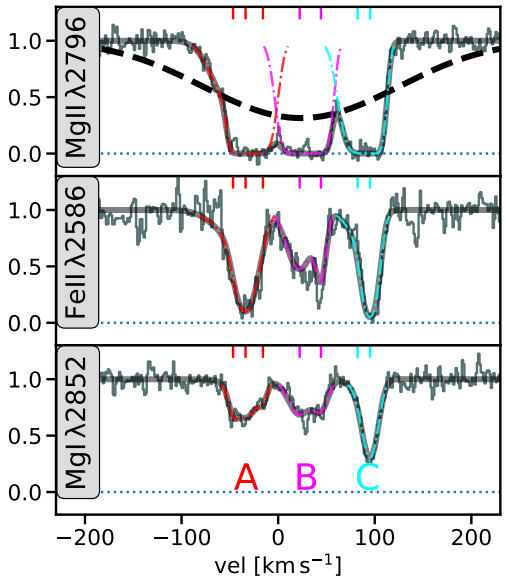

Figure 7. Absorption seen in the quasar UVES spectrum at the redshift of the *main* galaxy. Detected lines are transitions of Mg II, Mg I, and Fe II, for each of which one transition is shown. The thin grey line are the observed UVES data, while the thick line is a model fit to the data. This model consists of the seven components at velocities as indicated on the top. Three main kinematic components (A, B, C) can be visually identified, the contributions of which to the model are indicated by the red, magenta, and cyan lines, respectively. The black dashed line in the Mg II λ2796 panel is the UVES spectrum artificially degraded to the resolution of MUSE at this wavelength.

By selection we have a quasar sightline piercing through the halo of the *main* galaxy, at an impact parameter of 38.7 kpc. We describe the observed absorption in the quasar sightline in §5.1. In §5.2, we apply our generic outflow toy model (Bouché et al. 2012) to the observed quasar absorption. In addition to the quasar sightline, there are three background galaxies detected within 50 kpc of the *main* galaxy (see Fig. 1 (left)). The continuum of these galaxies is detected, but despite the depth of the MUSE observation, with relatively low S/N. We briefly summarize the limited information we can extract at the current depth from these sightlines in §5.3.

All four sightlines are just outside the region where we significantly detect Mg II emission, and hence allow us in principle to extend the mapping provided by the emission in an absorption tomographic way (e.g. Bowen et al. 2016; Lopez et al. 2018, 2019), especially if in the future observations of the background sources could be obtained with the ELTs.

5.1 Observed absorption in the quasar sightline

The UVES data for the quasar sightline allows us to study the absorption strength and kinematics not only for Mg II, based on which the system was selected, but also for several other transitions (Fig. 7). In addition to Mg II, we detect absorption in multiple Fe II lines and Mg I λ2852. Weaker lines from Zn II, Mn II, and Cr II, which would haved allowed us to constrain the dust content (e.g. De Cia et al. 2016; Wendt

et al. (2021)[paper V]), are covered but not significantly detected.

The Mg II absorption covers a velocity range from −96 to 125 km s^{-1} around the *main* galaxy's systemic redshift. As can be seen from the less saturated lines, the highest column densities appear to be in three main kinematic components. These three components are centered around −44, 23, and 95 km s^{-1} from the *main* galaxy's systemic redshift.[11]

We determined the Fe II and Mg I column densities using a multicomponent fitting approach as described in paper V, which uses the evolutionary algorithm of Quast et al. (2005) as used by Wendt & Molaro (2012). We find $\log(N_{\rm Fe II}/{\rm cm}^{-2}) = 14.5$ and $\log(N_{\rm Mg I}/{\rm cm}^{-2}) = 12.6$. While we cannot directly constrain the Mg II column density, as Mg II is strongly saturated, we can use two different approaches to obtain a crude estimate. One option is to assume a ratio between Mg II and Mg I that is typical for Mg II absorbers, which was found to be around 600:1 by Lan & Fukugita (2017). This would result in $\log(N_{\rm Mg II}/{\rm cm}^{-2}) = 15.4$. Another approach is to assume a typical dust depletion strength and pattern, which is necessary to estimate Mg from Fe. As found in paper V, sightlines along the galaxy's minor axis typically have [Zn/Fe] ≈ 0.8. For this [Zn/Fe] De Cia et al. (2016) find a difference between the Mg and Fe depletion strengths ($\delta_{\rm Fe} - \delta_{\rm Mg}$) of about -0.5. Combined with the difference between the Mg and Fe (solar) abundances of 0.1 dex, this results in $\log(N_{\rm Mg II}/{\rm cm}^{-2}) = 15.1$, consistent with the result starting from Mg I. While clearly both methods are very uncertain, the similarity of the estimates provides some confidence.

5.2 Modelled absorption in quasar sightline

The distribution of Mg II around galaxies is anisotropic, which can be explained with a two component picture consisting of an extended gas disk and a bi-conical outflow, as motivated in the introduction. The quasar sightline is along the *main* galaxy's minor axis ($\alpha = 87 \pm 1$ deg), and as such the absorption seen in this sightline is plausibly caused by outflowing gas.

Following Bouché et al. (2012), we try to match the velocity profile of the observed Mg absorption using a conical outflow with constant outflow velocity, $v_{\rm out}$, and (half-) opening angle $\theta_{\rm out}$. In paper III, we find typical values of 20–40 deg and ≈ 100–300 km s^{-1} for $\theta_{\rm out}$ and $v_{\rm out}$, respectively. In order to ensure mass conservation, the volume density of the considered ion, n, scales with r^{-2}, and is normalized at $r = 20$kpc (n_{20}). Here, r is the distance from the galaxy center. The orientation of the cones w.r.t. the quasar sightline is fully constrained by the orientation of the galaxy on the sky, except for the sign of the inclination. However, as the mean absorption velocity is - at least sightly - redshifted from the systemic redshift of the *main* galaxy, it seems more plausible that the sightline crosses the far cone.

Using our code CGMPY (see paper IV for a description), we calculated model absorption profiles for Mg II and Mg I and tried to find a parameter set ($v_{\rm out}$, $\theta_{\rm out}$, n_{20}) that qualitatively matches the observed profile. As Mg II is strongly saturated, we primarily compared model and data for the unsaturated Mg I. A model with $\theta = 35$ deg, $v_{\rm out} = 130$ km s^{-1}, $n_{20;\rm Mg I} = 2.1 \times 10^{-10}$cm^{-2} captures the overall velocity spread of the observed Mg I absorption (Fig. 8; lower right). As a consistency check, we also evaluated this model for Mg II (Fig. 8; upper right; red solid curve), where we assumed $n_{20;\rm Mg II}$ to be 600 times $n_{20;\rm Mg I}$ (c.f. §5.1; $n_{20;\rm Mg II} = 1.3 \times 10^{-7}$cm^{-3}), and found good agreement between model and data.

It is important to emphasize that we generally do not expect such model profiles to be a perfect match to the data, as the real distribution of Mg II is without doubt more complex than the smooth and coherent gas distribution and kinematics in our toy model. A first order correction that can often improve the similarity between observed and modelled outflow profiles (see paper III) is to assume a hollow cone, an assumption that is corroborated by observations of local galaxies (e.g. McKeith et al. 1995). However, the presence of absorption component B (see Fig. 7) suggests that the outflow cone around the *main* galaxy is not entirely hollow.

We note that a different model for the same system was presented in paper III. There, an additional outflow originating from the distant *secondary* galaxy was employed to explain the full absorption profile. However, with the refined galaxy redshift and inclination measurements in this present work, obtained with more accurate methodology possible thanks to the much deeper data now available (see §3), the outflow from the *main* galaxy alone appears sufficient to explain all the absorption.

Following Bouché et al. (2012) and Schroetter et al. (2015), we can use the model to calculate a mass outflow rate $\dot{M}_{\rm out}$. Using eq. 5 from paper III we find $\dot{M}_{\rm out} = 4\,{\rm M}_\odot\,{\rm yr}^{-1}$ with the parameters inferred above and assuming an H I column density $\log(N_{\rm H I}/{\rm cm}^{-2}) = 19.5 \pm 0.3$. The latter was obtained by using the relation between $EW_0^{\lambda 2796}$ and $N_{\rm H I}$ from Lan & Fukugita (2017), with the uncertainty on the $N_{\rm H I}$ being due to scatter in the relation. This yields a mass-loading factor $\eta \equiv \dot{M}_{\rm out}/SFR = 0.5$. This is a value at the lower end of the typical range at this redshift (e.g. Schroetter et al. 2015; Sugahara et al. 2017, paper III).

As a consistency check, we compared the density estimate from CGMPY to an analytical calculation. We estimated the Mg II column density, $\log(N_{\rm Mg II}/{\rm cm}^{-2}) \approx 15.0 - 15.5$, in §5.1 from the measured Mg I column density, $N_{\rm Mg I}$. The $N_{\rm Mg II}$ can then be converted for the assumed toy model geometry into a volume density using geometrical arguments, using eq. B5 from Bouché et al. (2012): [12]

$$N_{\rm Mg II} = \frac{n_{20} r_{20}^2}{b} 2\theta_{\rm out} \Rightarrow n_{20;\rm Mg II} = \frac{N_{\rm Mg II}}{2\theta_{\rm out}} \frac{b}{r_{20}^2} \quad (1)$$

We find $n_{20;\rm Mg II} \approx 5 \times 10^{-8}$ cm^{-3}, where we assumed $\theta_{\rm out} = 35$ deg. This is as expected about a factor two smaller than than the CGMPY estimate, as the CGMPY model does not take account of the sub-structure in the Mg I profile (Fig. 8 right).

[11] Velocities are based on Mg I.

[12] The equation assumes a background sightline crossing a conical outflow at $i = 90$ deg and $\alpha = 90$ deg, which is quite close to the configuration of the quasar sightline probing the halo of the *main* galaxy.

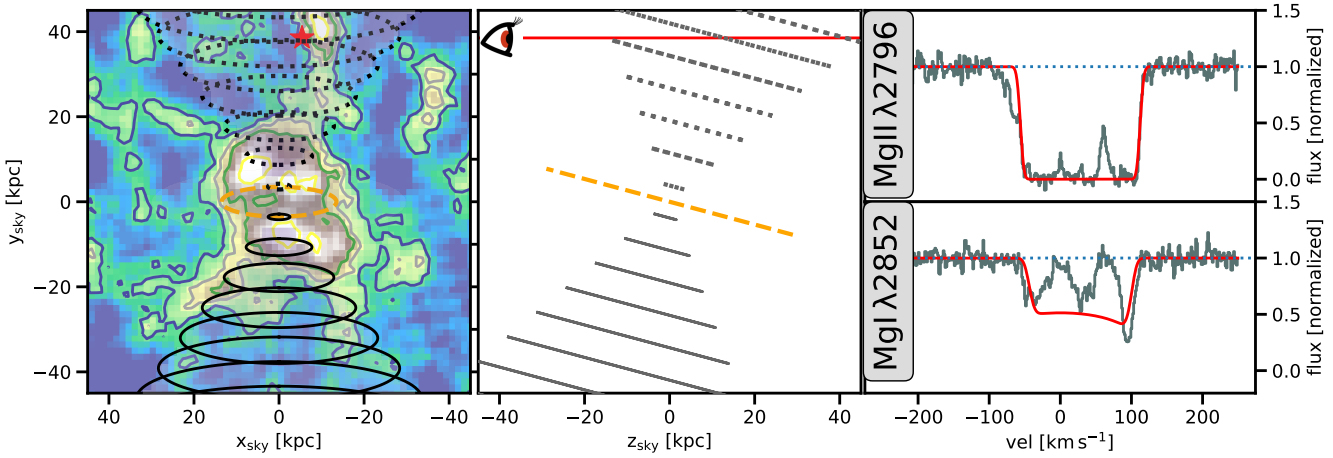

Figure 8. Toy model to explain the Mg absorption kinematics seen in the quasar sightline. **Left:** A front view of the toy bi-conical wind model overlayed on the Mg II emission surface brightness map from Fig. 1 (right) with the *main* galaxy's major axis aligned with the plot's x-axis. The disk of the central galaxy is indicated by a dashed orange ellipse. The black ellipses represent the orientation and extent of the bi-conical outflow model (see §6), where dotted ellipses represent the far cone, while solid ellipses show the near cone. The position of the quasar is indicated with a red star. **Center:** a side view of the bi-conical wind model, where the x-axis is parallel to the line-of-sight. The quasar sightline is shown in red, where the observer direction is indicated by the eye. **Right:** The absorption predicted by this model is overplotted in red on the Mg absorption observed in the UVES spectrum (grey) (Top: Mg II λ2796; Bottom: Mg I λ2582).

5.3 Observed absorption in galaxy sightlines

The three background galaxies within 50 kpc of the *main* galaxy (back_0p9, back_1p5, back_1p7) have at 4760 Å, which is the wavelength of Mg II at the redshift of the *main* galaxy, observed magnitudes of 24.8, 24.3, and 24.1, respectively. The coordinates and alignment of these galaxies with respect to the *main* galaxy are listed in Table 3.

The spectra of all three background sources are shown in Fig. 9, in addition to the quasar spectrum. Potential complications with using background galaxy spectra are photospheric and ISM/CGM absorption features intrinsic to the background galaxy, which by accident might coincide in the observed-frame wavelength with the absorption of interest in the foreground CGM. To test the presence of photospheric absorption features, we performed a full spectral fit with PPXF (Cappellari 2017) to each of the three background galaxies using the UV-extended E-Miles SSP (Vazdekis et al. 2016). The best-fit model, after normalising in the same way as the actual data, is shown as orange lines in Fig. 9. It is clear that the background galaxies' photospheric features are not important for the noise level of our data. ISM features, by contrast, are more problematic. In the case of back_1p7, there is C III] λλ1907, 1909 exactly at the observed wavelength of Mg II λ2796, making it impossible to fit this component of the Mg II doublet. For back_0p9 there is ISM/CGM absorption due to Fe II λ2852 at its redshift, but it is far enough in velocity from Mg II at the redshift of the *main* galaxy to not be problematic. In addition, both in back_0p9 and back_1p7 there is a component blueward of Mg II λ2796. However, this features seems absent in Mg II λ2803. Therefore, we could not convincingly identify this blueshifted absorption to be due to Mg II.

Due to the low S/N and the complications mentioned above, we refrained from quantitatively measuring the $EW_0^{\lambda 2796}$ and velocity centroid. Qualitatively, the data in all three sightlines, both the two more aligned with the major axis ($\alpha \lesssim 30$ deg) and the sightline more aligned with minor axis (back_0p9; $\alpha = 56$ deg), appear to have Mg II absorption consistent with being at least as strong as in the quasar sightline. This is especially the case for the closest of the three sightlines (back_1p7), which seems to have the strongest Mg II λ2803 absorption among the three sightlines. Given the known anti-correlation between $EW_0^{\lambda 2796}$ and b, this is not unexpected.

Kinematically, the Mg II λ2803 absorption seems to be relatively close to zero velocity. Depending on whether the blueshifted feature seen for Mg II λ2796 in the *back_1p7* and *back_0p9* sightlines is real, there might also be an additional blueshifted component. Interestingly, blueshifted absorption in sightlines *back_1p7* and *back_0p9* would be consistent with an extrapolation of the *main* galaxy's rotation field, and hence would provide further support for an extended rotating gas disk on CGM scales. However, given the low S/N, even deeper data will be necessary to confirm the blueshifted component and accurately measure the kinematics in these sightlines.

6 DISCUSSION OF Mg II EMISSION MORPHO-KINEMATICS

In this section, we discuss potential origins of the extended Mg II emission. One main focus of our discussion is to explore to what extent the generic toy model of a bi-conical outflow, which we used to interpret the absorption in §5.2, can also explain the observed emission morphology and kinematics. After an initial comparison of observed and predicted emission kinematics (§6.1), we discuss the feasibility of resonantly scattered continuum photons as a source of the Mg II emission (§6.2). For this assessment, we compare densities inferred from emission and absorption (§6.2.1) and test to

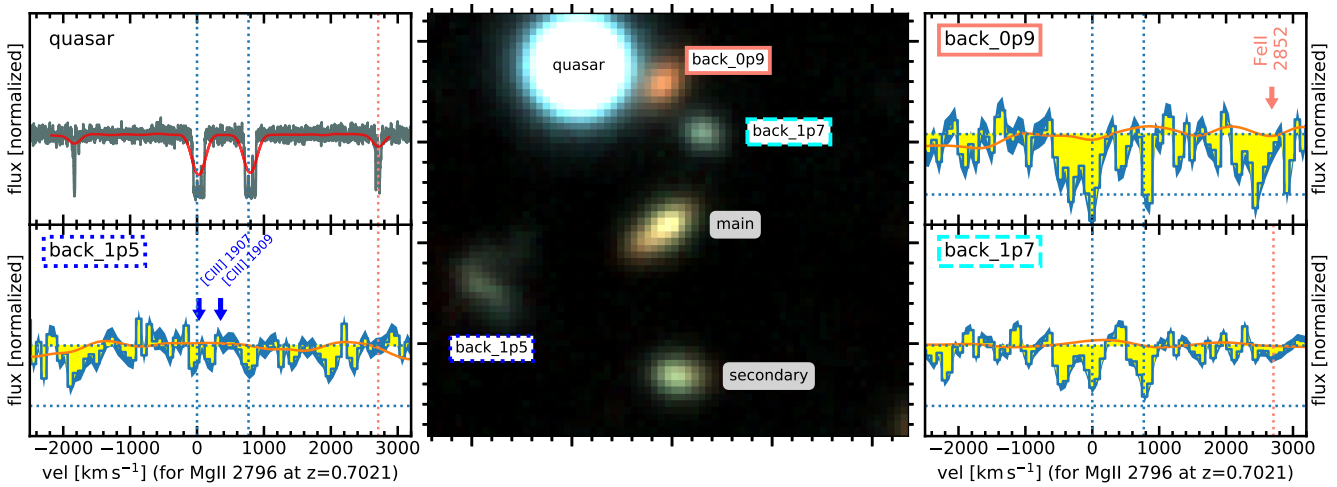

Figure 9. Mg II absorption from four background sightlines that probe the halo of the *main* galaxy. Shown is the wavelength region from 4720 Å to 4810 Å, which corresponds to a velocity range from −2500 km s^{-1} to 3200 km s^{-1} around Mg II λ2796 at $z = 0.7021$. **Center:** Zoom-in of Fig. 1 (left), which shows the position of the four background sources w.r.t. the *main* galaxy. **Upper Left:** UVES spectrum of the quasar sightline (grey). The red line also shows the UVES spectrum, but downgraded to the resolution of MUSE. **Lower Left, Lower & Upper Right:** The three background galaxy sightlines, back_1p5, back_0p9, back_1p7 as seen by MUSE. The orange line is a model obtained from a PPXF fit to the full spectral range covered by MUSE using the UV-extended E-Miles SSPs (Vazdekis et al. 2016). The spectral resolution of these models is by factors of 1.8, 2.5, and 2.7 lower than the data for back_0p9, back_1p5, and back_1p7, respectively. The blue dotted vertical lines in each of the four spectral panels indicate the positions of Mg II λ2796 and Mg II λ2803 at the redshift of the *main* galaxy. The back_1p5 galaxy spectrum has its C III] emission coincident with the wavelength of Mg II λ2796 in the *main* foreground galaxy, potentially masking the absorption. Furthermore, galaxy back_0p9 has at the edge of the shown wavelength range its Fe II λ2852 absorption. As galaxy back_0p9 is at a lower redshift than the three others sightlines, CGM Fe II λ2852 absorption at the redshift of *back_0p9* is possible in the other sightlines. The corresponding wavelength is indicated as the orange dotted-line.

what extent models with scattered continuum photons can reproduce the observed morphology (§6.2.2) and luminosity (§6.2.3). Finally, we discuss alternative mechanisms to produce the extended Mg II (and [O II]) emission (§6.3).

6.1 Mg II emission kinematics

As discussed in §4.2, the morphology of the CGM Mg II emission is dominated by two regions of strong emission along the galaxy's minor axis. Such a morphology is suggestive of a bi-conical outflow. To test the viability of this interpretation, some insight can be gained by comparing the observed emission kinematics (see §4.3) to that predicted from an idealized toy model.

In order to get an impression of the Mg II emission kinematics expected from our toy model, we used an extremely simple model: we assumed that each spatial point "emits" isotropically Mg II photons with an emissivity proportional to the Mg II density, $n_{\rm Mg II}$. Further, the photons escape from that point freely with the 2796/2803 ratio of 2:1, and are assumed to be emitted in the rest-frame of the outflowing Mg II ions. For a first model (Model A) we assumed a biconical outflow with the geometry, density, and velocity parameters set to those inferred from the Mg II absorption seen in the quasar sightline (see §5.2).

With these assumptions we created a simulated Mg II emission data cube, where we accounted for the appropriate MUSE PSF and line spread function, LSF, at the observed wavelength of Mg II. Subsequently, we created from this model cube a surface-brightness map in an identical way as described in §4.2 for the data. SB maps for both the data and this "Model A" are shown in the respective columns of Fig. 10's upper row. The overall flux normalization in the model was chosen arbitrarily so that the modelled emission approximately matches the observed SB. While the model SB map cannot reproduce the observations in detail, as expected from the extreme simplifications of the model, there are nevertheless similarities with the observations. E.g., the data SB map shows clear indications of a bi-conical structure as predicted by the model.

In the lower row of Fig. 10 "Data" ("Model A") we show a pseudo-longslit spectrum of the observed (modelled) Mg II emission for a slit aligned with the bi-conical structure. This slit is overplotted as a white dashed line on the observed (modeled) SB maps. The pseudo-longslit spectrum was created from a cube with the continuum of the galaxy and the quasar subtracted, as described in 4.1. The emission kinematics in the position-velocity-diagram, PVD, extracted from this pseudo-slit appear in approximate agreement between data and model. In particular, both data and model emission show a similar amount of red- and blueshift towards and away from the quasar, respectively. Further, the amount of the observed (and modelled) redshift of the Mg II emission in the direction of the quasar is consistent with the velocity of the Mg II absorption seen in the quasar (middle panel). Importantly, this means that the geometrical model can explain simultaneously the absorption kinematics in the quasar sightline and the emission kinematics.

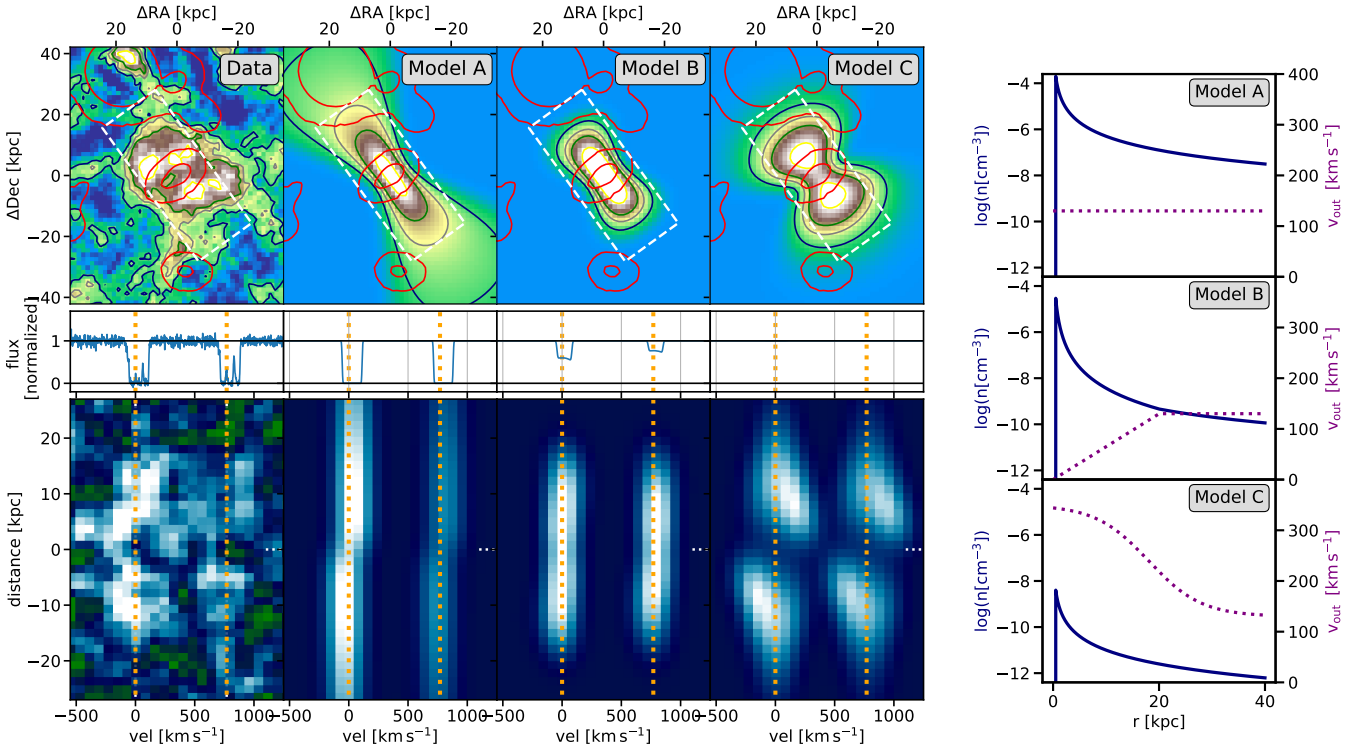

Figure 10. Kinematics of the Mg II emission along the *main* galaxy's minor axis. **Left:** The top panels show the spatial SB distribution of the observed ('Data') and modelled ('Model A-C') Mg II emission. The bottom panels show position-velocity diagrams (PVD) along the *main* galaxy's minor axis. These 2D spectra were extracted from the pseudo-slit shown with dashed-lines in the SB maps and have been smoothed with a tophat filter (r=1 pixel). Positive distances are towards the quasar. The zero point of the velocity scale in the plots is set to the wavelength of Mg II 2796 at the systemic redshift of the *main* galaxy. The two vertical orange dotted lines indicate the wavelengths expected for Mg II 2796 and Mg II λ2803, respectively. Both in the data and the models the Mg II emission appears blueshifted in the direction away from the quasar (*distance* < 0 kpc), while it is redshifted towards the quasar, consistent with the redshift seen in the quasar absorption. This absorption in the quasar sightline is shown in the middle panels on the same velocity scale as for the PVDs below. **Right:** The velocity and density profiles assumed for the three toy models shown in the left. 'Model A' (§6.1) assumes emissivity proportional to Mg II volume density and its parameters have been tuned to explain the absorption in the quasar sightline. 'Model B' (accelerating) and 'Model C' (decelerating) (§6.2.2), which assume physically motivated emissivity from continuum scattering, better reproduce the surface brightness distribution than 'Model A', but fail to reproduce the quasar absorption. The normalization of the maps has been been arbitrarily chosen (see §6.2.3).

6.2 Continuum scattering

6.2.1 Density estimate

We now turn to estimating the density of Mg II in the outflow from the extent of the emission. This requires a realistic treatment of the scattering optical depth as a function of the radius. Such an estimate can be obtained using the Sobolev approximation (Sobolev 1960; for applications in the context of CGM winds see e.g. Rubin et al. 2011; Martin et al. 2013; Prochaska et al. 2011; Scarlata & Panagia 2015; Carr et al. 2018).

The Sobolev approximation requires the presence of a velocity gradient, $|dv/dr|$, in the outflowing gas. This is important, as having a velocity gradient ensures that photons are only resonant within a small radial range. The characteristic thickness of this interaction region, the "Sobolev length", is then simply proportional to $s_0 = b_{\rm th}/|dv_{\rm out}/dr|_r$, where $b_{\rm th}$ is the thermal broadening of the line. If the "Sobolev" length is small compared to the extent of the wind, the "Sobolev" approximation holds. If the wind is furthermore only moving radially, as assumed here, and if the source at the centre can be approximated to be an isotropically emitting point source, the optical depth at a given radius can be approximated as:

$$\tau^s = \frac{\pi e^2}{m_e c} f_{\rm osc} \lambda_0 n_{\rm Mg II} \left|\frac{dv}{dr}\right|_r^{-1} = 4.54{\times}10^{-7}\,{\rm cm^3\,s^{-1}}\, n_{\rm Mg II} \left|\frac{dv}{dr}\right|_r^{-1} \quad (2)$$

Consequently, it is possible to estimate $n_{\rm Mg II}$ at a certain radius by inverting eq. (2), if τ^s and $|dv/dr|$ are known at this radius. Martin et al. (2013) argued that τ^s drops below one at the maximum extent of the observed emission. This assumes that the extent - ≈ 20 kpc in our case - is limited by the probability for scattering ($\propto {\rm e}^{-\tau_s}$) and not by the depth of the data. The assumption of $\tau^s = 1$ results in:

$$n_{\rm Mg II} = 2.2{\times}10^6\,{\rm cm^{-3}\,s} \left|\frac{dv}{dr}\right|_r = 7.1{\times}10^{-11}\,{\rm cm^{-3}} \left|\frac{dv}{dr}\frac{\rm kpc}{\rm km\,s^{-1}}\right|_r \quad (3)$$

If we assume, as an order-of-magnitude estimate, a velocity gradient of $|dv/dr| = 130\,{\rm km\ s^{-1}}/20\,{\rm kpc}$, as motivated by

the $v_{\rm out}$ inferred from the absorption (§5.2) and the observed extent of the emission. Then, eq. (3) gives a Mg II density at 20 kpc, $n_{20;\rm MgII}$, of 5×10^{-10} cm^{-3}.[13]

Thanks to the background quasar, we can alternatively constrain the gas density more directly from the absorption measured in the sightline. As described in §5.2, from the absorption we inferred $n_{20;\rm MgII} \approx 5 \times 10^{-8}$ cm^{-3}.[14] This density is a factor 100 larger than the value estimated here from the emission. Despite the relatively large uncertainties in both estimates, it might be difficult to explain such a large discrepancy.

Assuming that the emission-based estimate is wrong, one potential reason is the assumption of $\tau^s = 1$. However, a very high $\tau^s \approx 100$ would be required to consolidate absorption and emission. This seems inconsistent with the 2803/2796 flux ratio of 1.9±0.3 of the observed emission, as a line ratio closer to 1:1 should be expected for optically thick scattering. Another option would be an underestimated velocity gradient. While a velocity gradient a few times larger than the one assumed here is not ruled out by the emission data (see also 6.2.2), the difference can certainly not explain a substantial fraction of the discrepancy.

Assuming that the absorption-based estimate is wrong, a possible reason might be that the 'specific' sightline encounters more Mg II gas than a 'typical' sightline would. To asses this possibility, we compared the $EW_0^{\lambda 2796}$ of this sightline to those typical for sightlines around star-forming galaxies at $b \approx 40$ kpc. Due to the anisotropic distribution of Mg II (c.f. §1), it is important to restrict 'typical' here to sightlines along the minor axis. E.g., Lan & Mo (2018) find for minor axis sightlines at this impact parameter statistical values of about $EW_0^{\lambda 2796} \approx 1$–$2$ Å,[15] and we conclude that the $EW_0^{\lambda 2796}$ of our sightline (1.8 Å) is not exceptional.

6.2.2 *Emission kinematics and morphology from toy model*

In §6.1 we explored whether the toy model which we used to fit the absorption kinematics in the quasar sightline (see §5.2) can also explain the observed emission halo. There, we assumed that the emissivity is proportional to the density, an assumption which resulted in an unrealistic surface brightness profile, not surprisingly. Here, we explore models with scattering of the central galaxy's continuum photons by Mg II in the extended halo.

For the modelling of the continuum scattering we use the Sobolev optical depth (Eq. (2)) to obtain an estimate of the emissivity: a continuum photon in resonance with the Mg II transition will get scattered with a probability $1 - e^{-\tau^s}$. Assuming that the photon can escape after this single scattering, the local isotropic "emissivity", ϵ_{cs}, from a small volume element $dV = dA dr$ at radius r will be:

$$\epsilon_{cs} = \frac{L_\lambda}{4\pi r^2} \frac{\lambda_{0;r}}{c} (1 - e^{-\tau^s}) \left| \frac{dv}{dr} \right|_r dr\, dA \qquad (4)$$

where L_λ is the luminosity density of the central point source at the wavelength $\lambda_{0;r}$, with $\lambda_{0;r} = \lambda_0 \left(1 + \frac{v(r)}{c}\right)$. λ_0 is the resonant wavelength of the considered transition in the rest-frame of the central galaxy. Under this assumption of "emissivity" we created simulated cubes, SB maps and PVDs as described in §6.1.

As continuum scattering will only provide a viable source of Mg II emission if there is a velocity gradient, we can here not use the constant velocity profile assumed in "Model A" discussed in §6.1. Instead, we explore both accelerating and decelerating winds[16], as there is no consensus about the velocity profiles in cool outflows. Some observations prefer radially increasing velocities (e.g. Martin & Bouché 2009), while others support radially decreasing velocities (e.g. Martini et al. 2018; Burchett et al. 2021).

Given the relatively low S/N of the emission data and the simplifications of the model, we refrain from a futile attempt to formally constrain the geometry, density and velocity from the data. Instead, we simply show two feasible example models, one with increasing ('Model B') and one with decreasing velocity ('Model C') profile. Their velocity and density profiles are listed in Table 4 and are shown in the right panel of Fig. 10. We fixed the geometry to a biconocial outflow with $\theta_{\rm out} = 35$ deg for ('Model B'), as estimated from the quasar absorption in §5.2. By contrast, we used for 'Model C' a wide opening angle of $\theta_{\rm out} = 60$ deg, which is motivated by the extent of the observed emission. Further, we chose in these models the central luminosity, L_λ, so that resulting simulated halo surface-brightness is similar to the observed one. This choice is useful for comparing kinemat-

	Model A	Model B	Model C
$\rho(r)$	$c_{\rm a} \left(\frac{r}{r_0}\right)^{-2}$	$c_{\rm b} \left(\frac{r}{r_0}\right)^{-3}$ for $r < r_0$ $c_{\rm b} \left(\frac{r}{r_0}\right)^{-2}$ for $r \geq r_0$	$c_{\rm c} \left(\frac{r}{r_0}\right)^{-2}$
$v_{\rm out}(r)$	v_{const}	$\frac{{\rm d}v}{{\rm d}r}\, r$ for $r < r_0$ v_{const} for $r \geq 0$	$v_1 - \frac{v_2}{1+e^{-k(r-r_t)}}$

Table 4. Parametrizations of the density and velocity profiles shown in Fig. 10 (right) and used for the models shown in Fig. 10 (left). $c_{\rm a-c}$ are the density normalizations at r_0 of the respective models. The constant velocity (part) of model A (B) is $v_{const} = 130$km s^{-1}. The velocity gradient in the inner part ($r \leq r_0 < 20$kpc) of model B is ${\rm d}v/{\rm d}r = 6.5$ km s^{-1}/kpc. For Model C, $v_1 = 350$ km s^{-1}, $v_2 = 220$ km s^{-1}, $k = 0.2$ kpc^{-1}, and $r_t = 18$ kpc. To avoid numerical problems, we further set in all models the density for $r < 0.5$ kpc to zero.

[13] Assuming solar metallicity and neglecting depletion, this would correspond to $n_{\rm H} = n_{\rm MgII}/f_{\rm MgII}\, 10^{4.4} = 1.3 \times 10^{-5}\, cm^{-2}/f_{\rm MgII}$, with $f_{\rm MgII}$ being the Mg II ionization fraction.
[14] In the absorption modelling of §5.2 a scaling of $n \propto r^{-2}$ is assumed, which would be mass conserving only for an outflow with $v_{\rm out} = const$. By contrast, we assumed for the purpose of the Sobolev approximation a velocity gradient $v_{\rm out} \propto r$. This would require, if the mass in the cool phase is indeed conserved, $n \propto r^{-3}$. To reconcile the two assumptions, we could assume that $v_{\rm out} = const$ is valid beyond $r = 20$ kpc only.
[15] Lan & Mo (2018) state the sum of the 2796 and 2803 lines. Therefore, we divided their EW_0 values by 2, as for such high $EW_0^{\lambda 2796}$ both lines are typically saturated and the EW ratio is likely 1:1.

[16] Accelerating and decelerating does not necessarily mean that individual Mg II clouds change their velocity. The velocity profile is here simply the radial profile of the ensemble of clouds.

ics and morphology between data and model. We critically compare these required L_λ to the available L_λ in §6.2.3.

Model B has a constant velocity gradient out to 20 kpc, beyond which it has a constant velocity. The resulting SB map and velocity profile (see Fig. 10) are similar to the data. While the modelled SB map does not show the central suppression as in the data, the suppression in the data might be the consequence of Mg II absorption in the continuum of the central galaxy (see §4.2). We note that a decelerating wind with the same absolute velocity gradient, the same density profile, and the same $\theta_{\rm out}$ as 'Model B' would also have the same surface brightness profile as 'Model B'. Therefore, we used for the sake of variation in 'Model C', in addition to a large $\theta_{\rm out}$(=60 deg), a radially changing velocity gradient that is steepest off-centre from the galaxy. Having the steepest gradient off-centre results even for the chosen monotonically declining density profile in the surface brightness peaking away from the centre. This two-lobe geometry is very reminiscent of the observed SB distribution without the absorption correction. Further, 'Model C' has a relatively high velocity of 350 km s^{-1} in the centre. Such a relatively high velocity in the inner part seems still consistent with the data (see Fig. 10 left lower), and data and model seem to agree remarkably well, especially in the direction away from the quasar.

In summary, the simple continuum scattering models with a biconical outflow geometry seem to be able to reproduce kinematics and, at least approximately, the SB distribution of the observations. Both models with increasing and decreasing velocity gradients seem consistent with the data. As expected from the discussion in §6.2.2, densities which allow for low enough scattering optical depths to support the observed 2:1 Mg II doublet ratio result for the assumed monotonously declining density profiles in too low densities at the position of the quasar sightline to explain the observed absorption (see middle row of Fig. 10).

6.2.3 Mg II *luminosity*

For the continuum scattering models discussed in §6.2.2 and shown in Fig. 10, we arbitrarily chose the strength of the central continuum source so that the models matched the observed MgII SB brightness in the halo. This required continuum fluxes, f_λ, which exceeded the observed ones by factors of $\approx$ 20 and $\approx$ 10 for models B and C, respectively. This discrepancy between model and observations can be understood: The maximum flux from continuum scattering is naturally limited by the number of continuum photons available for scattering. This budget is determined both by the strength of the continuum, f_λ, and the range of radial velocities of the ouflowing Mg II ions ($\Delta v = \max(v_{\rm out}(r)) - \min(v_{\rm out}(r))$), as scattering happens in the rest-frame of the ions. For a non-isotropic biconical outflow with (half-)opening angle $\theta_{\rm out}$, the maximum Mg II flux is further reduced by a factor $1 - \cos\theta_{\rm out}$. This results in:

$$f_{\rm MgII} = 2(1-\cos\theta_{\rm out})\Delta v \frac{\lambda_{obs}}{c} f_\lambda \quad (5)$$

where the factor 2 accounts for Mg II being a doublet[17]. For our fiducial $\theta_{\rm out} = 35$ deg and $f_\lambda = 2 \times 10^{-18}$erg s^{-1} cm^{-2} Å^{-1} at the wavelength of Mg II, this results in $f_{\rm MgII} = 1.15 \times 10^{-18}$erg s^{-1} cm^{-2} for an outflow with $\Delta v = 100$ km s^{-1}. For comparison, the total measured flux in the Mg II halo is 41×10^{-18}erg s^{-1} cm^{-2}, which is a factor 30–40 larger than the expected one.

We briefly consider three possibilities that could reduce the tension between required and available continuum photons. First, a Δv of up to $\approx$ 500km s^{-1}, might be consistent with the data, if the high velocity gas is only close to the galaxy (c.f. 'Model C'). However, even with $\Delta v = 500$km s^{-1} the discrepancy would still be a factor $\approx$ 7. Second, the effective cone opening angle might be larger than the assumed $\theta_{\rm out} = 35$ deg, especially in the inner part. In the extreme case of an isotropic wind ($\theta_{\rm out} = 90$ deg) the flux would be a factor 5 larger than for the assumed $\theta_{\rm out} = 35$ deg. Third, the f_λ escaping the ISM in direction of the cone might be larger than the f_λ measured from the edge on view of the galaxy, due to less dust extinction in direction perpendicular to the disk. However, it is unlikely that the difference is much more than a magnitude (factor 2.5) (e.g. Yip et al. 2010; Chevallard et al. 2013). Finally, more realistic radiative transfer accounting for multiple scattering could result in the preferential escape of scattered photons towards the observer (perpendicular to the cone). An investigation of this possibility is beyond the scope of this paper.

6.3 Alternative origins of the extended emission

As discussed in §6, a biconical outflow model where Mg II ions scatter continuum photons emitted from the central galaxy can, at least approximately, reproduce the morphology of the Mg II nebula and simultaneously explain the kinematics of halo gas seen in emission and absorption. However, it results in inconsistent density estimates between emission and absorption §6.2.1 and struggles to reproduce the Mg II luminosity of the nebula §6.2.3.

One way to boost the number of photons available for scattering on the Mg II ions in the CGM would be if the galaxy produces Mg II line emission in its H II regions. While Mg II emission from H II regions is certainly feasible (e.g. Erb et al. 2012; Feltre et al. 2018), the amount of Mg II emission originating from the ISM of the *main* galaxy appears low, even when correcting for potential down-the-barrel absorption (see Fig. 4). Given that the statistical presence or absence of Mg II emission does not depend on the galaxy's inclination (Finley et al. 2017b), it appears unlikely that the Mg II emission flux escaping the *main* galaxy's ISM perpendicular to the disk is much larger than suggested by our edge-on observations.

Therefore, it is unavoidable to consider, in addition to scattering, also in-place production of Mg II photons in the halo. Further support for at least a partial non-scattering origin of extended Mg II emission comes from the presence of clear extended emission also in the non-resonant oxygen lines (see §4.4). Extended line emission from optical non-resonant

[17] The factor 2 will get modified if Δv is larger than the separation of the doublet (= 770 km s^{-1}).

lines produced in the cool-warm ionized phase of galactic-scale winds seems indeed common, as seen around local starbursts, such as M82 (Lynds & Sandage 1963; Bland & Tully 1988; Heckman et al. 1990; Sharp & Bland-Hawthorn 2010).

In the outflows around local starbursts the line ratios of the various observed lines are more consistent with shocks than with H II regions photo-ionized by stars (e.g. Heckman et al. 1990). The lack of access to important diagnostic lines (e.g. [O I], [N II]) does not allow us to conclusively decide whether shocks are responsible for the extended emission around the *main* galaxy. Nevertheless, we can still test for feasibility by comparing the strength of the observed lines to shock model predictions (including precursor). We used the Allen et al. (2008) model grid in the updated version by Alarie & Morisset (2019) using MAPPINGS V. For a preshock density of $n = 1\mathrm{cm}^{-3}$, the grid includes models with shock velocties between 100 and 1000 km s^{-1}, magnetic fields between $10^{-4}$and 10 μG, and five different abundance sets. We find that only models (shock + precursor) with low shock velocities ($\approx 100-200$km s^{-1}) can explain the observed low [O III]/[O II] ratio of $\approx 1/3$. The velocities seem plausible as they are similar to the dispersion of the Mg II emission. Models with these velocities predict, independently of magnetic field strength, a Mg II/[O II] ratio of $\approx 1/2$ (assuming LMC abundances). While the observed ratio of ≈ 1 is somewhat higher, the predicted ratio is close enough when considering that Mg II might also have a contribution from scattering. Further, we can compare the surface brightness predicted by such shocks to the one observed for the Mg II nebula. Those models with acceptable [O III]/[O II] emit Mg II from their shock surface with $\approx 10^{-5}$–10^{-4} erg s^{-1} cm^{-2}. Assuming that shock surfaces cover the full area of the nebula, this would correspond for the $z = 0.7$ halo to an observed Mg II SB of $\approx 10^{-18}$–10^{-17}erg s^{-1} cm^{-2} arcsec^{-2}. Interestingly, this is of the same order as the observed SB (see Fig. 3). This means that emission by shocks could be a viable source of the extended [O II] and Mg II emission.

Motivated by the biconical geometry of the Mg II halo (§4.2) and the measured kinematics (§4.3), the observations appear very consistent with an outflow. However, the extended metal-enriched gas could also (partially) originate from tidal stripping or from intergalactic transfer via outflows from a neighboring galaxy (e.g. Anglés-Alcázar et al. 2017; Mitchell et al. 2020). While the *main* galaxy does not appear to be in a dense group, in which extended emission from non-resonant lines has been observed also outside the local Universe (Epinat et al. 2018; Johnson et al. 2018; Chen et al. 2019), the presence of the *secondary* galaxy in the proximity of *main* and its off-centre star-forming clump (see Appendix A2) make intergalactic transfer and tidal stripping plausible alternative contributions to the extended cool gas.[18] Certainly, starburst-driven outflows and tidally stripped gas will often co-exist. As the signatures of outflows and stripped gas could be similar at the level of our $z = 0.7$ observations, it does not yet seem feasible to conclusively rule out that there are other contributions to the extended emission than a pure outflow from the *main* galaxy.

[18] We note that the Mg II SB map (Fig. 1 right) shows potentially a weak "bridge" between the *main* and *secondary* galaxy. However, we consider it more likely to be residuals from the subtraction of the *secondary* galaxy than a real tidal feature.

7 CONCLUSION & DISCUSSION

The main focus of this paper was to report the first discovery of a Mg II emission halo around a galaxy near a quasar sightline, using deep (11.2 hr) VLT/MUSE data from the MEGAFLOW survey. The main findings are:

- The $z = 0.702$ *main* galaxy is a typical main-sequence galaxy with $\log(M_*/\mathrm{M}_\odot) = 10.05^{+0.15}_{-0.11}$ and SFR=$22.8^{+15.4}_{-19.0}$ M$_\odot$ yr^{-1} ($\delta(MS) = 0.4^{+0.3}_{-0.5}$), but has a relatively large inclination with $i \simeq 75$deg. The galaxy has a minor companion at 32 kpc (less than 1/5 of M_* of the *main* galaxy);
- We detect Mg II $\lambda\lambda$ 2796, 2803 emission around this galaxy that extends to a projected radius of 25 kpc and covers 1.0×10^3 kpc^2 above a surface brightness of 14×10^{-19} erg s^{-1} cm^{-2} arcsec^{-2} (2σ) (Fig.1 right);
- The Mg II emission is not isotropic, but is strongest along the galaxy's projected minor axis (Fig. 3). Similarly, we detect extended [O II] emission along the minor axis (Figs. 3 & 6);
- The minor axis Mg II emission kinematics is blue- and redshifted on opposite sides of the galaxy's major axis, respecitvely (Figs. 5 & 10);
- The quasar sightline, which is aligned with the galaxy's minor-axis, has strong Mg II absorption ($EW_0^{\lambda 2796} = 1.8$ Å) at an impact parameter of 39 kpc whose kinematics is consistent with the Mg II emission (Fig. 7 & 10) ;
- We identified three background galaxies within 50 kpc of the *main* galaxy. While we see indications of Mg II absorption at the redshift of our halo in these sightlines, they lack the S/N to infer kinematical information from these sightlines (Fig. 9);
- The kinematics of the gas seen in both the emission and the quasar absorption are consistent with the expectation from a simple toy model of a bi-conical outflow (Fig. 8 & 10);
- We estimated the CGM Mg II density both from the emission - under the assumption of continuum scattering - and the quasar absorption, and find values discrepant by two orders of magnitude. Further, continuum scattering struggles to explain the brightness of the halo.
- Shocks in the outflow are a viable alternative to explain the missing Mg II photons and the non-resonant extended [O II] emission.

We put the main emphasis of this paper on characterizing the kinematics, of both the Mg II absorption and emission. While we also tried to gain some insight into understanding the morphology and luminosity of the emission nebula through comparison of simple scattering toy models (Sobolev approximation) and shock models, further analysis should profit from the use of full radiative transfer models for the resonant Mg II (e.g. Prochaska et al. 2011; Michel-Dansac et al. 2020; Burchett et al. 2021). Given the complex morphology and kinematics seen in this Mg II halo, radiative transfer simulations will likely need to go beyond the computationally efficient assumption of spherical symmetry, and

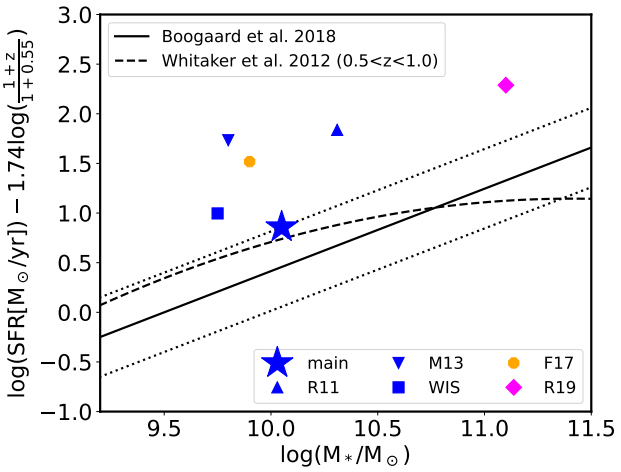

Figure 11. Galaxies with Mg II halos in the SFR–M_* plane compared to the main-sequence of star-formation (MS). In blue are the four Mg II halo objects found so far (*main*: this work, SFR from [O II]; WIS: Wisotzki et al. in prep, SFR from Hβ; R11: Rubin et al. 2011 (=Burchett et al. 2021), SFR from Hβ; M13: Martin et al. 2013, SFR from [O II]). In addition, a galaxy with a Fe II* halo but no Mg II emission (F17: Finley et al. 2017a, SFR from [O II]) and a galaxy with a gigantic [O II] halo and potentially slightly extended Mg II emission (R19, Rupke et al. 2019, SFR from SED) are indicated. All SFRs have for comparability been corrected to a reference $z = 0.55$, using the evolution of the MS normalization as found by Boogaard et al. (2018). For comparison both the MS of Boogaard et al. 2018 and Whitaker et al. 2012 are shown.

adopt a bi-conical structure. After all, there is now strong evidence from Mg II absorption in background sightlines that an anisotropic Mg II distribution in the CGM is a generic property around star-forming galaxies (see §1). Further, it might be necessary to consider more realistic galaxy models than an isotropically emitting point source.

Understanding and inferring accurate information from the morphology and kinematics of Mg II halos will be one of the main challenges in the emerging field of Mg II halos, with some such efforts already made in this paper and in previous studies (e.g. Rubin et al. 2011; Prochaska et al. 2011; Martin et al. 2013; Burchett et al. 2021).

Another important, more phenomenological way to characterize Mg II halos will be to understand around which type of galaxies they occur. In Fig. 11, we compare the position of the four Mg II halos so far published in the literature in the SFR–M_* plane. While the first two detections (Rubin et al. 2011; Martin et al. 2013), which are based on long-slit observations,[19] were significantly above the main-sequence of star-forming galaxies (MS; e.g. Whitaker et al. 2012; Boogaard et al. 2018) and could be considered as starbursts, the galaxy in Wisotzki et al. in prep. has only slightly enhanced star-formation (about 2σ above the MS). The *main* galaxy presented in this paper is even within the 1σ scatter of the MS. Therefore, it is clear that a starburst, at least at the time of the observation, is not a requirement for a Mg II halo to occur. On the other hand, even being significantly above the MS and having spatially extended emission in another line does not necessitate the presence of a halo. E.g. in a starburst with extended Fe II* emission in the MUSE data no extended Mg II emission was found (Finley et al. 2017a), and in a starburst surrounded by a giant [O II] nebula (Rupke et al. 2019), which is the largest metal line nebula around a galaxy detected so far, only slightly extended Mg II was found.

A specific inclination seems also not to be a requirement for the presence of Mg II halos. While the *main* galaxy discussed in this work has a very high inclination ($i \approx 75$ deg), the galaxy at the center of the halo in the Wisotzki et al. in prep. is likely seen almost face on ($i \approx 0$ deg). Nevertheless, the difference in inclination can explain a major difference between the two objects in the Mg II spectrum extracted for the central galaxy. We did not detect any strong Mg II absorption in the observed down-the-barrel spectrum of the *main* galaxy, while the object of Wisotzki et al. shows a typical P-Cygni profile. Even when correcting for potential infilling by emission (see §4.2), the absorption is not very strong ($EW_0^{\lambda 2796} \approx 0.8$ Å). The lack of strong down-the-barrel absorption for galaxies observed at high inclination, such as the *main* galaxy, is expected for a bi-conical cool outflow launched perpendicular to the galaxy disk and this expectation has been statistically confirmed (e.g. Kornei et al. 2012; Rubin et al. 2014; Bordoloi et al. 2014).

A potential similarity between the Mg II halo objects is that they have non-relaxed disturbed morphologies due to clumps, potentially but not necessarily triggered by past or present mergers. Both the *main* galaxy and the object from Martin et al. (2013) lack Hubble Space Telescope data data, which will be necessary to gain further insight into this issue. Fortunately, it will soon be possible to study the requirements for the presence or absence of Mg II halos more systematically, thanks to the quickly increasing amount of available wide-field IFU data from MUSE and KCWI.

ACKNOWLEDGEMENTS

We thank the referee for a constructive report, which helped to improve the quality of the manuscript. This study is based on observations collected at the European Southern Observatory under ESO programmes 095.A-0365(A), 096.A-0609(A), 0100.A-0089(A), 0101.A-0287(A). This work has been carried out thanks to the support of the ANR FOGHAR (ANR-13-BS05-0010), the ANR 3DGas-Flows (ANR-17-CE31-0017), and the OCEVU Labex (ANR-11-LABX-0060). FL and TG acknowledge support from ERC starting grant ERC-757258-TRIPLE. SC gratefully acknowledges support from Swiss National Science Foundation grants PP00P2_163824 and PP00P2_190092, and from the European Research Council (ERC) under the European Union's Horizon 2020 research and innovation programme grant agreement No 864361. JB acknowledges support by Fundação para a Ciência e a Tecnologia (FCT) through the research grants UID/FIS/04434/2019, UIDB/04434/2020, UIDP/04434/2020 and through the Investigador FCT Contract No. IF/01654/2014/CP1215/CT0003. This work made use of the following open source software: GALPAK^{3D} (Bouché et al. 2015), ZAP (Soto et al. 2016), MPDAF (Piqueras

[19] Burchett et al. (2021) is a re-observation with the KCWI IFU of the Rubin et al. (2011) object.

et al. 2017), MATPLOTLIB (Hunter 2007), NUMPY (van der Walt et al. 2011), ASTROPY (Astropy Collaboration et al. 2013).

DATA AVAILABILITY

The data underlying this article were accessed from the ESO archive (`http://archive.eso.org`; program IDs 095.A-0365(A), 096.A-0609(A), 0100.A-0089(A), 0101.A-0287(A)). The derived data generated in this research will be shared on reasonable request to the corresponding author.

REFERENCES

Alard C., Lupton R. H., 1998, ApJ, 503, 325
Alarie A., Morisset C., 2019, Rev. Mex. Astron. Astrofis., 55, 377
Allen M. G., Groves B. A., Dopita M. A., Sutherland R. S., Kewley L. J., 2008, ApJS, 178, 20
Anglés-Alcázar D., Faucher-Giguère C.-A., Kereš D., Hopkins P. F., Quataert E., Murray N., 2017, MNRAS, 470, 4698
Astropy Collaboration et al., 2013, A&A, 558, A33
Bacon R., et al., 2015, A&A, 575, A75
Bacon R., et al., 2017, A&A, 608, A1
Bacon R., et al., 2021, A&A, 647, A107
Bland J., Tully B., 1988, Nature, 334, 43
Boogaard L. A., et al., 2018, A&A, 619, A27
Bordoloi R., et al., 2011, ApJ, 743, 10
Bordoloi R., et al., 2014, ApJ, 794, 130
Borisova E., et al., 2016, ApJ, 831, 39
Bouché N., Hohensee W., Vargas R., Kacprzak G. G., Martin C. L., Cooke J., Churchill C. W., 2012, MNRAS, 426, 801
Bouché N., Murphy M. T., Kacprzak G. G., Péroux C., Contini T., Martin C. L., Dessauges-Zavadsky M., 2013, Science, 341, 50
Bouché N., Carfantan H., Schroetter I., Michel-Dansac L., Contini T., 2015, AJ, 150, 92
Bouché N., et al., 2016, ApJ, 820, 121
Bowen D. V., Chelouche D., Jenkins E. B., Tripp T. M., Pettini M., York D. G., Frye B. L., 2016, ApJ, 826, 50
Bruzual G., Charlot S., 2003, MNRAS, 344, 1000
Burchett J. N., Rubin K. H. R., Prochaska J. X., Coil A. L., Vaught R. R., Hennawi J. F., 2021, ApJ, 909, 151
Cai Z., et al., 2017, ApJ, 837, 71
Calzetti D., Armus L., Bohlin R. C., Kinney A. L., Koornneef J., Storchi-Bergmann T., 2000, ApJ, 533, 682
Cappellari M., 2017, MNRAS, 466, 798
Carr C., Scarlata C., Panagia N., Henry A., 2018, ApJ, 860, 143
Chabrier G., 2003, PASP, 115, 763
Chen H.-W., Kennicutt Robert C. J., Rauch M., 2005, ApJ, 620, 703
Chen H.-W., Helsby J. E., Gauthier J.-R., Shectman S. A., Thompson I. B., Tinker J. L., 2010, ApJ, 714, 1521
Chen H.-W., Boettcher E., Johnson S. D., Zahedy F. S., Rudie G. C., Cooksey K. L., Rauch M., Mulchaey J. S., 2019, ApJ, 878, L33
Chevallard J., Charlot S., Wandelt B., Wild V., 2013, MNRAS, 432, 2061
Claeyssens A., et al., 2019, MNRAS, 489, 5022
Daddi E., et al., 2010, ApJ, 713, 686
De Cia A., Ledoux C., Mattsson L., Petitjean P., Srianand R., Gavignaud I., Jenkins E. B., 2016, A&A, 596, A97
Dekker H., D'Odorico S., Kaufer A., Delabre B., Kotzlowski H., 2000, Design, construction, and performance of UVES, the echelle spectrograph for the UT2 Kueyen Telescope at the ESO Paranal Observatory. pp 534–545, doi:10.1117/12.395512
Dijkstra M., Kramer R., 2012, MNRAS, 424, 1672
Epinat B., et al., 2012, A&A, 539, A92
Epinat B., et al., 2018, A&A, 609, A40
Erb D. K., Quider A. M., Henry A. L., Martin C. L., 2012, ApJ, 759, 26
Erb D. K., Steidel C. C., Chen Y., 2018, ApJ, 862, L10
Feldmeier J. J., et al., 2013, ApJ, 776, 75
Feltre A., et al., 2018, A&A, 617, A62
Finley H., et al., 2017a, A&A, 605, A118
Finley H., et al., 2017b, A&A, 608, A7
Francis P. J., et al., 2001, ApJ, 554, 1001
Freundlich J., et al., 2013, A&A, 553, A130
Freundlich J., Bouché N. F., Contini T., Daddi E., Zabl J., Schroetter I., Boogaard L., Richard J., 2021, MNRAS, 501, 1900
Heckman T. M., Armus L., Miley G. K., 1990, ApJS, 74, 833
Ho S. H., Martin C. L., 2020, ApJ, 888, 14
Ho S. H., Martin C. L., Kacprzak G. G., Churchill C. W., 2017, ApJ, 835, 267
Hunter J. D., 2007, Computing in Science and Engineering, 9, 90
Johnson S. D., et al., 2018, ApJ, 869, L1
Kacprzak G. G., Churchill C. W., Ceverino D., Steidel C. C., Klypin A., Murphy M. T., 2010, ApJ, 711, 533
Kacprzak G. G., Churchill C. W., Barton E. J., Cooke J., 2011, ApJ, 733, 105
Kacprzak G. G., Churchill C. W., Nielsen N. M., 2012, ApJ, 760, L7
Kacprzak G. G., et al., 2014, ApJ, 792, L12
Kamann S., Wisotzki L., Roth M. M., 2013, A&A, 549, A71
Kassin S. A., et al., 2007, ApJ, 660, L35
Kewley L. J., Dopita M. A., 2002, ApJS, 142, 35
Kornei K. A., Shapley A. E., Martin C. L., Coil A. L., Lotz J. M., Schiminovich D., Bundy K., Noeske K. G., 2012, ApJ, 758, 135
Lan T.-W., Fukugita M., 2017, ApJ, 850, 156
Lan T.-W., Mo H., 2018, ApJ, 866, 36
Lan T.-W., Ménard B., Zhu G., 2014, ApJ, 795, 31
Lanzetta K. M., Bowen D., 1990, ApJ, 357, 321
Laursen P., Sommer-Larsen J., Andersen A. C., 2009, ApJ, 704, 1640
Leclercq F., et al., 2017, A&A, 608, A8
Leclercq F., et al., 2020, A&A, 635, A82
Lopez S., et al., 2018, Nature, 554, 493
Lopez S., et al., 2019, MNRAS, p. 2763
Lynds C. R., Sandage A. R., 1963, AJ, 68, 284
Maiolino R., et al., 2008, A&A, 488, 463
Martin C. L., Bouché N., 2009, ApJ, 703, 1394
Martin C. L., Shapley A. E., Coil A. L., Kornei K. A., Bundy K., Weiner B. J., Noeske K. G., Schiminovich D., 2012, ApJ, 760, 127
Martin C. L., Shapley A. E., Coil A. L., Kornei K. A., Murray N., Pancoast A., 2013, ApJ, 770, 41
Martin C. L., Ho S. H., Kacprzak G. G., Churchill C. W., 2019, ApJ, 878, 84
Martini P., Leroy A. K., Mangum J. G., Bolatto A., Keating K. M., Sandstrom K., Walter F., 2018, ApJ, 856, 61
McKeith C. D., Greve A., Downes D., Prada F., 1995, A&A, 293, 703
Michel-Dansac L., Blaizot J., Garel T., Verhamme A., Kimm T., Trebitsch M., 2020, A&A, 635, A154
Mitchell P. D., Schaye J., Bower R. G., 2020, MNRAS, 497, 4495
Moffat A. F. J., 1969, A&A, 3, 455
Momose R., et al., 2014, MNRAS, 442, 110
Muzahid S., Kacprzak G. G., Churchill C. W., Charlton J. C., Nielsen N. M., Mathes N. L., Trujillo-Gomez S., 2015, ApJ, 811, 132
Nielsen N. M., Churchill C. W., Kacprzak G. G., Murphy M. T., 2013, ApJ, 776, 114

Nielsen N. M., Churchill C. W., Kacprzak G. G., Murphy M. T., Evans J. L., 2015, ApJ, 812, 83
Peng C. Y., Ho L. C., Impey C. D., Rix H.-W., 2010, AJ, 139, 2097
Piqueras L., Conseil S., Shepherd M., Bacon R., Leclercq F., Richard J., 2017, arXiv e-prints, p. arXiv:1710.03554
Prescott M. K. M., Dey A., Jannuzi B. T., 2009, ApJ, 702, 554
Prescott M. K. M., Momcheva I., Brammer G. B., Fynbo J. P. U., Møller P., 2015, ApJ, 802, 32
Prochaska J. X., Kasen D., Rubin K., 2011, ApJ, 734, 24
Quast R., Baade R., Reimers D., 2005, A&A, 431, 1167
Rahmani H., et al., 2018a, MNRAS, 474, 254
Rahmani H., et al., 2018b, MNRAS, 480, 5046
Rickards Vaught R. J., Rubin K. H. R., Arrigoni Battaia F., Prochaska J. X., Hennawi J. F., 2019, ApJ, 879, 7
Rubin K. H. R., Weiner B. J., Koo D. C., Martin C. L., Prochaska J. X., Coil A. L., Newman J. A., 2010, ApJ, 719, 1503
Rubin K. H. R., Prochaska J. X., Ménard B., Murray N., Kasen D., Koo D. C., Phillips A. C., 2011, ApJ, 728, 55
Rubin K. H. R., Prochaska J. X., Koo D. C., Phillips A. C., Martin C. L., Winstrom L. O., 2014, ApJ, 794, 156
Rupke D. S. N., et al., 2019, Nature, 574, 643
Saintonge A., et al., 2013, ApJ, 778, 2
Scarlata C., Panagia N., 2015, ApJ, 801, 43
Schlegel D. J., Finkbeiner D. P., Davis M., 1998, ApJ, 500, 525
Schmidt K. B., et al., 2019, A&A, 628, A91
Schroetter I., Bouché N., Péroux C., Murphy M. T., Contini T., Finley H., 2015, ApJ, 804, 83
Schroetter I., et al., 2016, ApJ, 833, 39
Schroetter I., et al., 2019, MNRAS, 490, 4368
Schroetter I., et al., 2020, arXiv e-prints, p. arXiv:2012.04935
Sharp R. G., Bland-Hawthorn J., 2010, ApJ, 711, 818
Sobolev V. V., 1960, Moving envelopes of stars
Soto K. T., Lilly S. J., Bacon R., Richard J., Conseil S., 2016, ZAP: Zurich Atmosphere Purge (ascl:1602.003)
Steidel C. C., Adelberger K. L., Shapley A. E., Pettini M., Dickinson M., Giavalisco M., 2000, ApJ, 532, 170
Steidel C. C., Kollmeier J. A., Shapley A. E., Churchill C. W., Dickinson M., Pettini M., 2002, ApJ, 570, 526
Steidel C. C., Bogosavljević M., Shapley A. E., Kollmeier J. A., Reddy N. A., Erb D. K., Pettini M., 2011, ApJ, 736, 160
Sugahara Y., Ouchi M., Lin L., Martin C. L., Ono Y., Harikane Y., Shibuya T., Yan R., 2017, ApJ, 850, 51
Tacconi L. J., et al., 2010, Nature, 463, 781
Tacconi L. J., et al., 2013, ApJ, 768, 74
Tumlinson J., Peeples M. S., Werk J. K., 2017, ARA&A, 55, 389
Vazdekis A., Koleva M., Ricciardelli E., Röck B., Falcón-Barroso J., 2016, MNRAS, 463, 3409
Verhamme A., Schaerer D., Maselli A., 2006, A&A, 460, 397
Weilbacher P. M., Streicher O., Palsa R., 2016, MUSE-DRP: MUSE Data Reduction Pipeline (ascl:1610.004)
Weilbacher P. M., et al., 2020, A&A, 641, A28
Weiner B. J., et al., 2009, ApJ, 692, 187
Wendt M., Molaro P., 2012, A&A, 541, A69
Wendt M., Bouché N. F., Zabl J., Schroetter I., Muzahid S., 2021, MNRAS, 502, 3733
Whitaker K. E., van Dokkum P. G., Brammer G., Franx M., 2012, ApJ, 754, L29
Wisotzki L., et al., 2016, A&A, 587, A98
Wisotzki L., et al., 2018, Nature, 562, 229
Yang Y., Zabludoff A., Tremonti C., Eisenstein D., Davé R., 2009, ApJ, 693, 1579
Yip C.-W., Szalay A. S., Wyse R. F. G., Dobos L., Budavári T., Csabai I., 2010, ApJ, 709, 780
Zabl J., Freudling W., Møller P., Milvang-Jensen B., Nilsson K. K., Fynbo J. P. U., Le Fèvre O., Tasca L. A. M., 2016, A&A, 590, A66
Zabl J., et al., 2019, MNRAS, 485, 1961

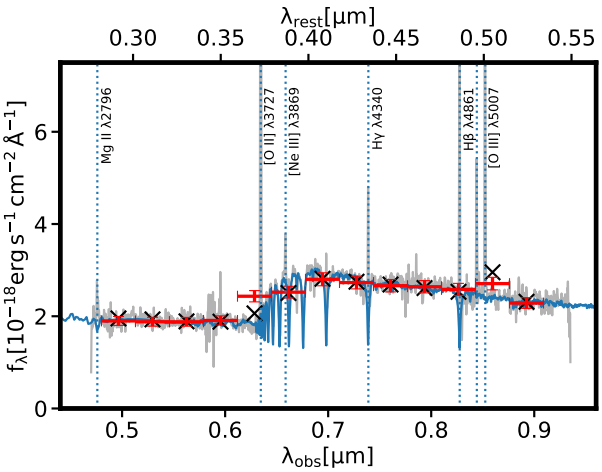

Figure A1. SED fit for the *main* galaxy. The blue curve shows the best-fit SED model, while the grey curve is the observed spectrum (smoothed with a Gaussian of width $\sigma = 1.5$ pixel). The SED fit was done to photometry in 13 medium band filters represented by the red horizontal error bars. While the red error bars are plotted at the measured flux density, the black crosses show the flux density predicted by the best-fit SED model, which includes the contribution from emission lines.

Zabl J., et al., 2020, MNRAS, 492, 4576
van der Walt S., Colbert S. C., Varoquaux G., 2011, Computing in Science and Engineering, 13, 22

APPENDIX A: GALAXY PROPERTIES

A1 Stellar masses

We determined the stellar masses of the galaxies using our custom SED fitting code CONIECTO (Zabl et al. 2016). Identical to earlier papers in the MEGAFLOW series, we fit BC03 (Bruzual & Charlot 2003) models to photometry determined from 13 pseudo-medium filters optimized to cover the full MUSE wavelength range. The width of these filters is shown by the red horizontal error bars in Fig. A1. As in paper IV, we use here a delayed-tau star-formation history.

The the stellar mass obtained from the SED fit (shown in Fig. A1) for the *main* galaxies is $\log(M_\star/M_\odot) = 10.05^{+0.15}_{-0.11}$. The *secondary* galaxy has $\log(M_\star/M_\odot) = 9.29^{+0.22}_{-0.04}$. This means that the *secondary* galaxy has less than 1/5 the mass of the *main* galaxy and can be considered as a minor companion to the *main* galaxy.

A2 Morphology

In order to characterize the morphology of the *main* galaxy, we use a combination of broad- and narrow-band maps. Fig. A2 shows an [O II] flux map (upper left), an [O III] flux map (upper center), and a color composite created from three broadband filters (lower right), using the 'best-seeing' cube from Section 2.

Looking first at the lower right image in Fig. A2, one can see that the galaxy is redder towards the south-east and bluer towards the north-west. This redder region could have an older stellar population or more dust. Unfortunately, the

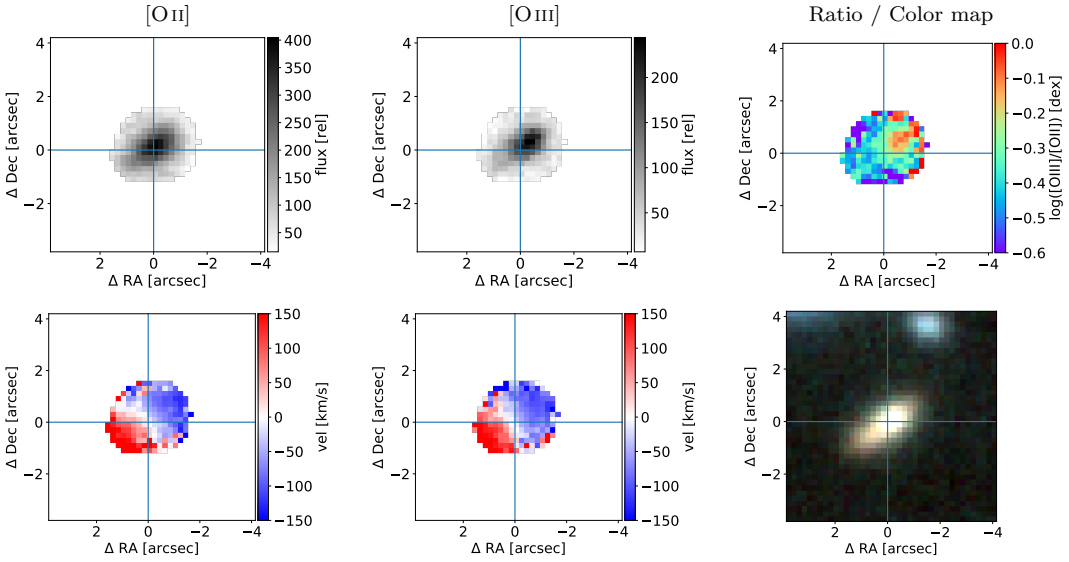

Figure A2. Flux and kinematic maps. The blue cross is in all six panels at the same position. This position indicates the location we define as the formal centre of the galaxy throughout the paper. **Left and Centre:** The [O II] and [O III] flux (top) and velocity (bottom) maps have been determined by fitting the respective emission lines in each spaxel using the CAMEL code. To increase the S/N the cube has been sligtly smoothed in the spatial direction with a FWHM of 1 pix before fitting. **Upper right:** Ratio between the [O III] and [O II] flux maps. The ratio appears to increase towards the north-west. **Lower right:** RGB image using i', r', and V filters. The continuum has an extension towards the south-east, which is only weakly visible in the emission lines. The blue galaxy near the top is a background galaxy (back_1p7). All figures in this panel are based on the data cube created from the best-seeing data only.

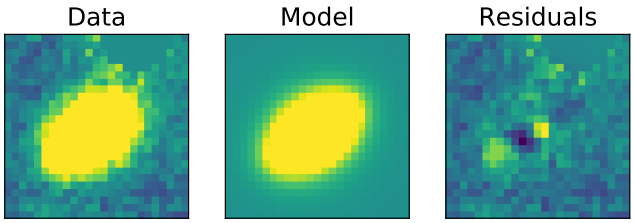

Figure A3. Comparison between data and GALFIT model for a broadband image (r') of the *main* galaxy. All the data, the model, and the residuals (data-model) are scaled identically. The cutouts have a size of $5'' \times 5''$.

S/N of Hγ is not sufficient to allow for a spatially resolved dust map from Hγ/Hβ (Hα is not covered).

From Fig. A2, a more striking variation is between the spatial distribution of [O II] $\lambda\lambda$3727, 3729 (top left) and [O III] λ5007 (top middle), where [O III] is enhanced compared to [O II] towards the north-west. The [O III]/[O II] ratio map (upper right panel of Fig. A2) makes this apparent. This difference can be caused by variations in the ionization parameter, q, and/or the gas metallicity (e.g. Kewley & Dopita 2002). Together, the [O III]/[O II] map and the color map indicate that this galaxy has a large clump of enhanced SFR, slightly offset ($\delta x = 0.5$ kpc) from the galaxy center. [20]

Because the *main* galaxy contains this significant clump of SFR and because [O II] is also extended towards the minor axis, the inclination from [O II] will be biased. We thus revert to fitting the continuum to estimate the morphological parameters of the *main* galaxy. Fig. A3 shows the best-fit single-Sérsic model obtained with GALFIT (Peng et al. 2010) to an r' broadband image created from the MUSE cube and using a Moffat PSF with the parameters as measured from the quasar. This best-fit model has a Sérsic index of 0.50, an axis ratio of 0.25 ($i \approx 75.7$ deg), and a half-light radius $R_e = 4.6$ kpc.

A3 Kinematics

The bottom left and middle panels of Fig. A2 show the [O II] and [O III] velocity fields determined using the CAMEL code (Epinat et al. 2012). The rotation field is consistent between both [O II] and [O III] and looks undisturbed.

As discussed in Appendix A2, the line flux distribution deviates from a Sérsic profile due to the presence of a SFR clump, and thus prevents us from perform a simultaneous fit of the morphology and kinematics with GALPAK^{3D}. We thus first perform a two component (two Sérsics, one representing the clump) model fit with GALFIT (Peng et al. 2010) on the [O III] NB image, where the PSF resolution is higher than [O II]. [O III] is also preferred as the [O III] SB profile extends little beyond the continuum (see Fig. 3) and the fit gives hence a good representation of the star-forming ISM. Subsequently, we use this intrinsic two component flux profile, with the two components independently scaled to [O II], and the inclination inferred from the continuum fit (Appendix A2) as input when we perform the 3D kinematic modelling using GALPAK^{3D} (Bouché et al. 2015).

[20] Alternatively, the galaxy could be undergoing a minor merger.

Table A1. Line fluxes as measured with PPXF.

Ion	λ (obs) [Å]	λ (rest) [Å]	line flux [10^{-18}erg s^{-1} cm^{-2}]
[O II]	6344	3727	71.0±0.8
[O II]	6349	3730	104.4±1.6
H I	6420	3772	1.2±0.5
H I	6466	3799	1.9±0.4
H I	6530	3836	9.0±0.3
[Ne III]	6587	3870	8.7±0.4
H I	6621	3890	7.6±0.4
Hδ	6984	4103	14.3±0.5
Hγ	7390	4342	26.6±0.5
Hβ	8277	4863	62.0±0.7
[O III]	8443	4960	24.9±0.3
[O III]	8525	5008	76.3±0.5

A4 Line fluxes and metallicity

We measured line fluxes using the PPXF code, which allows to simultaneously fit a stellar continuum model and the emission lines. For the continuum we allowed an arbitrary linear combination of single age BC03 stellar populations models, convolved to the wavelength-dependent spectral resolution of MUSE. All fit emission lines were assumed to be Gaussians with the intrinsic velocity dispersion shared between the different transitions. While we imposed on [O II] λ3729/[O II] λ3727 and [O III] λ4959/[O III] λ5007 constraints from atomic physics,[21] the ratio between all others lines was allowed to freely vary. The resulting fit is shown in Fig. A4 and the fluxes are listed in Table A1.

The measured fluxes, after de-reddening assuming a Calzetti et al. (2000) extinction curve and an E(B–V) = 0.29 as estimated from the stellar mass (see Table 2), allow us to use several of the common strong-line gas-phase metallicity indicators, except those involving [N II], which is not covered by our MUSE data. Using the calibrations from Maiolino et al. (2008), we have estimated the oxygen abundance, 12+log(O/H), with five different indicators using ratios between the [O II], [O III], Hβ, and [Ne III] lines (see Fig. A5). The combination of the five indicators prefers a $12 + \log(\mathrm{O/H}) \approx 8.7$–$8.8$, indicating approximately solar abundance. This means that the *main* galaxy is a typical galaxy on the mass-metallicity relation at $z = 0.7$. We note that the agreement between the different indicators could be improved by assuming a lower E(B–V) ≈ 0.2. This could indicate that the E(B–V) estimate as obtained from the E(B–V)-M_* relation might be a slight overestimate.

APPENDIX B: Mg II SB MAP FOR WIDE FILTER

We investigated whether using a broad NB filter (2270 km s^{-1}; yellow in Fig. 2) instead of the double NB filter (2×600 km s^{-1}; blue in Fig. 2) does have a substantial impact on the Mg II morphology of the halo. The left panel of Fig. B1 shows the SB map for the wide filter, while the right panel shows the difference between this map and the map for the double NB filter, as shown in Fig. 1 (right). We can conclude that the morphology does not substantially change when using a wider filter. As a narrower filter has lower noise and less problems with continuum residuals from other sources in the field, we therefore decided to use the double NB filter also for extraction of the radial SB profiles in Fig. 3.

APPENDIX C: ABSENCE OF ROTATION IN OUTFLOW REGIONS

In §4.3 we found that the kinematics in the two outer minor-axis regions (6 & 8 in Fig. 5) are consistent with the expectation from a biconical outflow, with redshifted emission in region 8 and blueshifted emission in region 6. However, as the emission flux in the outer part of the cone-like regions is not completely symmetric w.r.t. the galaxy's minor axis, the kinematic signature could in principle also be caused by a (very) extended, clumpy, co-rotating disk: In region 8 the Mg II emission is slightly brighter on the redshifted side of the galaxy rotation field, while in region 6 it is somewhat brighter on the blue-shifted side. To rule out rotation as explanation for the kinematics in these regions, we split regions 6 & 8 into two halves each, split by the galaxy's minor axis. The regions and the spectra extracted from these regions are shown in Fig. C1, where the "b" and "r" regions are on the blue- and redshifted side of the galaxy rotation field, respectively. We find that in both cases "b" and "r" have the same velocity sign, which strongly supports the outflow scenario. Furthermore, this result tentatively indicates that the outflow does not carry high angular momentum.

This paper has been typeset from a TEX/LATEX file prepared by the author.

[21] $0.28 < [\mathrm{O\,II}]\,\lambda3729/[\mathrm{O\,II}]\,\lambda3727 < 1.47$ and $[\mathrm{O\,III}]\,\lambda4959/[\mathrm{O\,III}]\,\lambda5007 = 0.33$.

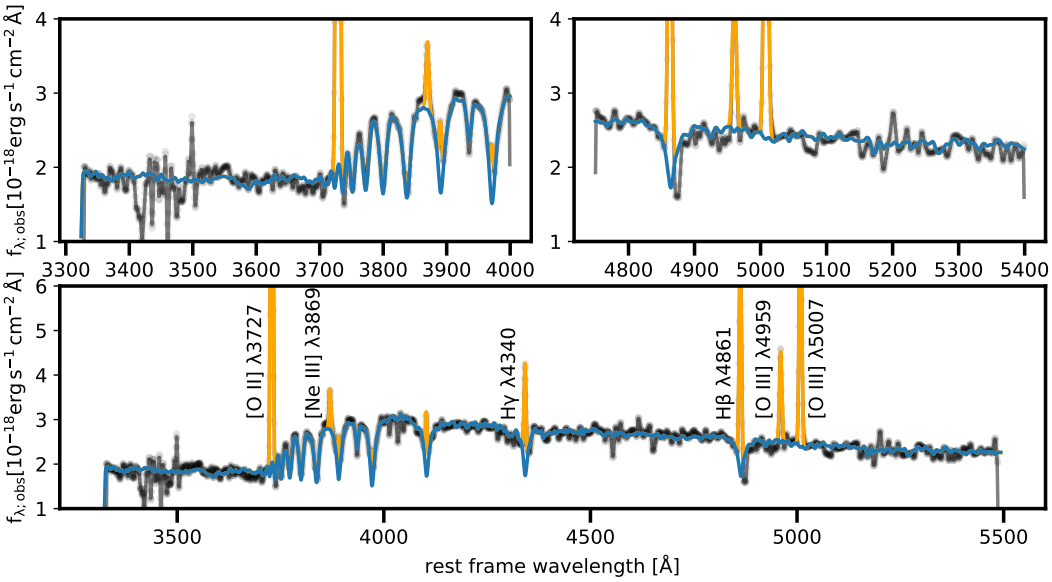

Figure A4. Nebular and stellar decomposition using PPXF for the *main* galaxy. The data (black) are fit by a combination of BC03 stellar population models (blue) and emission lines (orange). The two upper panels are zooms into the lower panel.

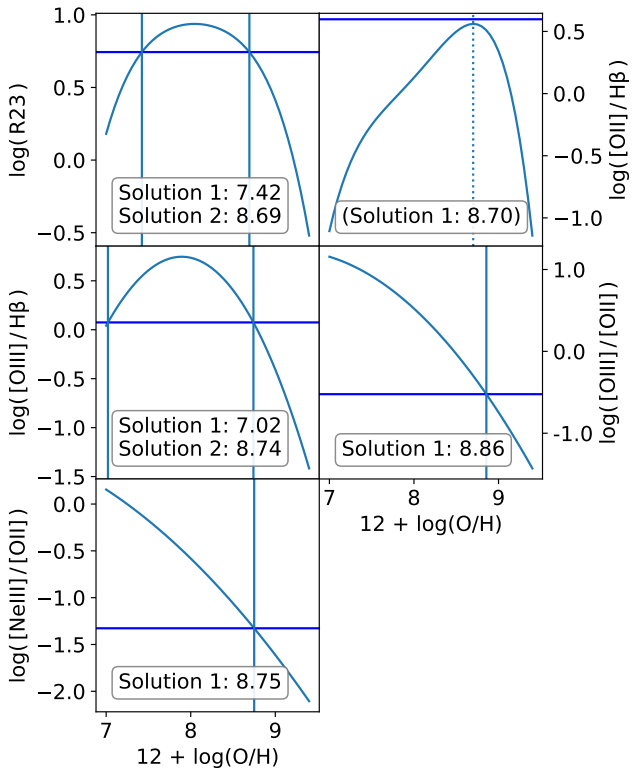

Figure A5. Oxygen gas-phase metallicity estimates using the strong-line calibrations from (Maiolino et al. 2008).

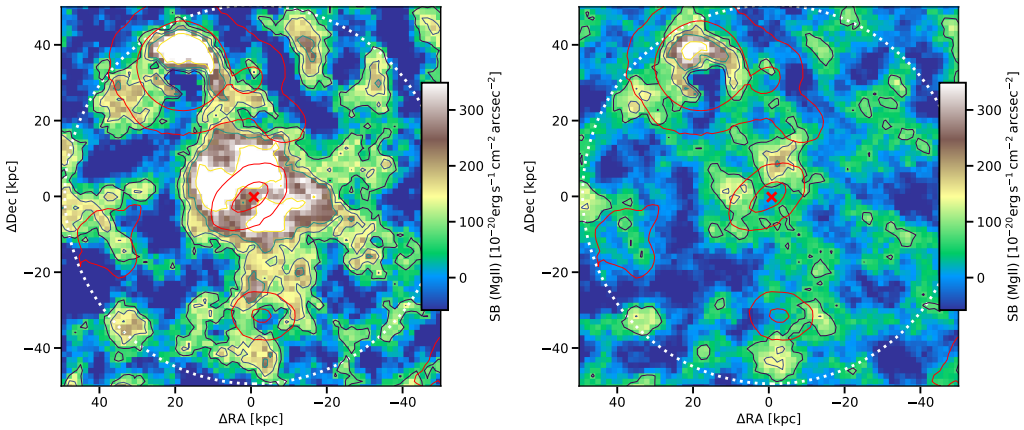

Figure B1. **Left:** MgII SB emission map as in Fig. 1 (right), but using instead of the double NB filter ($2 \times 600\,\mathrm{km\ s^{-1}}$; blue in Fig. 2) a broad single filter ($2270\,\mathrm{km\ s^{-1}}$; yellow in Fig. 2). **Right:** The difference between the wide-filter SB map and the map based on the double NB as in Fig. 1 (right) is shown. The contour levels are in both panels at the same SB levels as in Fig. 1 (right). The flux at the position of the quasar is likely a residual from the quasar PSF subtraction and not real emission.

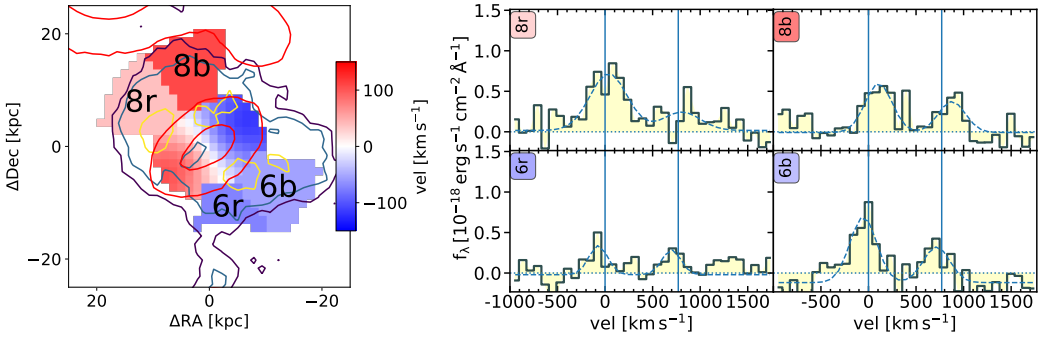

Figure C1. MgII spectra extracted from the numbered regions shown in the left panel are shown in the right panel. These regions split the two outer minor axis regions from Fig. 5 into the part where the extrapolation of the galaxy rotation field would be blueshifted ("b") and the part where it would be redshifted ("r"). A fit to the MgII doublet in each of the four regions is shown as blue-dashed line. The v_{los} from this fit sets the color-scale of the regions in the map. The galaxy rotation field measured from [OII] with GALPAK^{3D} is shown in the centre of the map.